Large-scale infra-slow dynamics of extracellular potentials linked to synchronous states revealed by graphene neural probes

Garcia-Cortadella, R.[1,2], *Cisneros-Fernandez, J.*[3], *Schwesig, G.*[1], *Shahidi, A.*[1], *Umurzakova, A.*[1], *Schäfer, N.*[2], *Aguilar, J.*[3], *Masvidal-Codina, E.*[2,3], *Del Corro, E.*[2], *Moahrlok, R.*[4], *Kurnoth, M.*[4], *Paetzold, J.*[4], *Loeffler, H.*[4], *Jeschke, C.*[4], *Meents, J.*[4], *Illa, X.*[3], *Serra-Graells, F.*[3], *Guimerà-Brunet, A.*[3], *Garrido, J. A.*[2,5]*, *Sirota, A.*[1]*

1. Bernstein Center for Computational Neuroscience Munich, Faculty of Medicine, Ludwig-Maximilians Universität München, Planegg-Martinsried, Germany
2. Catalan Institute of Nanoscience and Nanotechnology (ICN2), CSIC and BIST, Campus UAB, Bellaterra, 08193, Barcelona, Spain
3. Centro de Investigación Biomédica en Red en Bioingeniería, Biomateriales y Nanomedicina (CIBER-BBN), Madrid, Spain
4. Multi Channel Systems MCS GmbH, Reutlingen, Germany
5. ICREA, Pg. Lluís Companys 23, 08010, Barcelona, Spain

* Corresponding authors

Abstract

Brain states exhibit slow transitions that are coordinated by slowly varying homeostatic and neuromodulatory factors. These infra-slow dynamics modulate neuronal excitability, giving rise to brain state-specific synchronous faster oscillatory patterns across brain regions. Such synchronous states could be reflected in local infra-slow variations in the extracellular local field potential (LFP), providing new insights into the organisation of spontaneous brain dynamics beyond the established fast time scales. However, mapping of the LFP dynamics across brain regions with high spatio-temporal resolution remains challenging, particularly in capturing the elusive infra-slow component. To overcome these limitations, we developed neural probes based on arrays of up to 512 multiplexed graphene transistors, which enable DC-coupled, high-density, and large-scale recordings of surface and translaminar cortical activity in freely behaving rats. Analysis of cortex-wide topographic patterns of fast (1-50 Hz) oscillation dynamics improves segmentation, provides new insights into global brain states and allows detection of the local oscillatory states. We find that synchronous oscillatory brain states of variable scale and duration, ranging from slow wave sleep (SWS), high voltage spindles and sleep spindles during SWS are associated with corresponding topographically and translaminar structured DC potential shifts, which manifest as infra-slow fluctuations in the LFP. We propose a unified qualitative model for the emergence of DC potentials from synchronous dynamics mediated by the sustained gradient of extracellular K^+. This study shows that infra-slow spatio-temporal patterns in LFP mirror spatially organized oscillatory dynamics, reflecting the interplay between sub-cortical inputs and cortical excitability.

Introduction

Large-scale synchronous network dynamics provide the temporal scaffold for integration and segregation of distributed computation in the brain[1,2] and is shaped by various physiological processes including neuromodulatory dynamics, metabolic and homeostatic factors that vary at infra-slow (<0.5 Hz) scale[3–7]. These dynamics modulate neuronal intrinsic properties, excitability and effective connectivity and thereby the emergent synchronous neuronal dynamics across the brain at various time scales from seconds to minutes. Infra-slow excitability fluctuations, related to the level of arousal, have been shown to shape brain state transitions[6,8–11], constraining complex spatiotemporal brain dynamics to a low-dimensional latent space[12–14]. Infra-slow brain dynamics are also reflected in diverse observables, such as neural population[11,15] and neuromodulatory dynamics[6,16–18], hemodnamics[19–21] and fluctuations in membrane potential[22] or calcium concentration[23]. Synchronous dynamics in laminar networks is reflected in the LFP signals originating from collective local or volume-conducted transmembrane currents[24,25]. Infra-slow dynamics in the LFP, mostly in the form of DC shifts, have been reported since the middle of last century[26] in relation to spontaneous transitions between physiological brain states[27–29], state changes induced by stimulation[30–32], as well as pathological states, such as epileptic seizures, spreading depression or metabolic disfunction[33–40]. However, detailed characterization of the infra-slow LFP (isLFP) and identification of its origin has been limited due to measurement polarity and source ambiguity, limited spatial coverage and coarse resolution[21,33,36,40,41]. Furthermore, the ubiquity of these signals calls for a re-evaluation of their association with the distributed state-related changes of the neural synchrony rooted in the underlying infra-slow modulatory dynamics.

Despite the potential role of infra-slow dynamics in coordinating brain-wide activity across spatio-temporal scales[8,11,22,23,42–45], current brain large-scale recording technologies do not enable full-band mapping across large brain areas with submillimeter resolution. On the one hand, optical and magnetic imaging techniques present a limited temporal resolution and are often not suitable for chronic experiments in freely moving animals, which are required for the investigation of unconstrained brain states and behavioural dynamics. On the other hand, large-scale electrophysiological recordings are limited in their sensitivity at very low frequencies or suffer from poor spatial resolution. One potential approach to address this technical challenge is to upscale the number of channels in micro-ECoGs while enhancing their sensitivity in the DC/infra-slow band. However, despite recent advances in high channel count flexible micro-electrocorticography (ECoG) arrays[46–51], DC-coupled LFP mapping across large cortical areas with high spatial resolution has been out of reach so far. Overcoming this barrier could provide a unique window into both infra-slow spatio-temporal dynamics and the origin of the associated isLFP signals. This, in turn, would yield a novel insight into the role of infra-slow brain dynamics in coordinating neural synchronization across the brain at different temporal scales[5,8,25], linking research in small animal models and non-invasive imaging studies in humans[9,42,45].

In this study, we leverage large-scale multiplexed graphene transistor arrays to overcome this central challenge in neuroimaging. Recent advances in graphene technology showed that graphene solution-gated field-effect transistors (g-SGFETs) are promising building blocks for high-channel-count neural probes. Previous studies showed that they are suitable both for DC-coupled chronic recordings in freely moving rodents[40,52,53] and for operation in multiplexed mode[54–56]. We employ a combination of these key features enabling large-scale, up to 512 channels, and high spatio-temporal resolution mapping of DC-coupled signals in freely moving chronically implanted rats. We demonstrate the

seamless combination of multiplexed ECoGs with multiplexed depth graphene probes for the simultaneous recording of epi-cortical and intra-cortical DC-coupled LFP across behavioral and brain states.

Dense cortex-wide long-term LFP recordings enable detection, classification and characterization of both global brain states and local sleep spindles based on high dimensional spatio-spectral features. Cortex-wide and depth-resolved DC and infra-slow components of the LFP reveal a distinct topographic and translaminar pattern of the DC potential associated with the synchronous oscillatory states, that was common for hypersynchronous high voltage spindles (HVS), as well as transitions from slow-wave sleep (SWS) and infra-slow fluctuations within SWS associated with global upregulation of sleep spindles. Topographic and translaminar features of these infra-slow potentials are consistent with a qualitative model that provides a unified mechanistic link between neuronal synchronization states and the emergence of a topographic and layer-specific sustained gradient in extracellular K^+ concentration[57,58], which leads to the generation of cortex-wide translaminar dipole via the electrogenic Na-K pump activation that gives rise to the observed isLFP signal pattern. Our study opens the door to the use of multiplexed graphene probes for high spatio-temporal resolution neural interfaces with implications in clinical and fundamental neuroscience research, from the detection of pathological states to the understanding of large-scale neuronal synchronization dynamics.

Results

Graphene-based active neural probes and dedicated recording systems

Graphene transistors operate as transducers, converting extracellular potentials into current variations between the drain and the source (Fig. 1a). This sensing mechanism, together with the graphene's electrochemical stability, enables high-quality DC-coupled recordings, avoiding amplifier saturation and minimizing drifts[52]. Furthermore, transistors can be arranged in addressable arrays, enabling the implementation of time-domain multiplexing[55,56]. Implementing the read-out circuitry at the output of the rows of the arrays and sequentially switching the drain-to-source bias across columns reduces the complexity of connectors and enables up-scaling the number of channels[56] (Fig. 1a).

Here, we demonstrate the use of custom-built electronics for the operation of high-count transistor arrays in freely moving rats. We show the operation of an open-source system with 256 channels for early adoption of the technology[56], as well as a headstage based on an application-specific integrated circuit (ASIC)[54] to enhance the channel count scalability, reaching 512 channels in freely moving rats (Fig. 1a, Methods and Extended Data Fig. 1). In multiplexed operation, the graphene probes presented a median equivalent noise at the gate of 3.4µV (Q1= 2.8µV and Q3=6.0µV) per frequency decade (see Extended Data Fig. 2 for a detailed characterization). Furthermore, we demonstrated the embedding of addressable transistor arrays into narrow linear probes (Fig. 1b), integrating 32 channels in a 106µm wide probe consisting of 3 metal layers[40,59,60]. In this manner, ECoGs and depth probes could be seamlessly combined and operated with the same recording system (by sharing read-out blocks and sampling resources), enabling DC-coupled, dense recordings across cortical layers simultaneously with surface recordings.

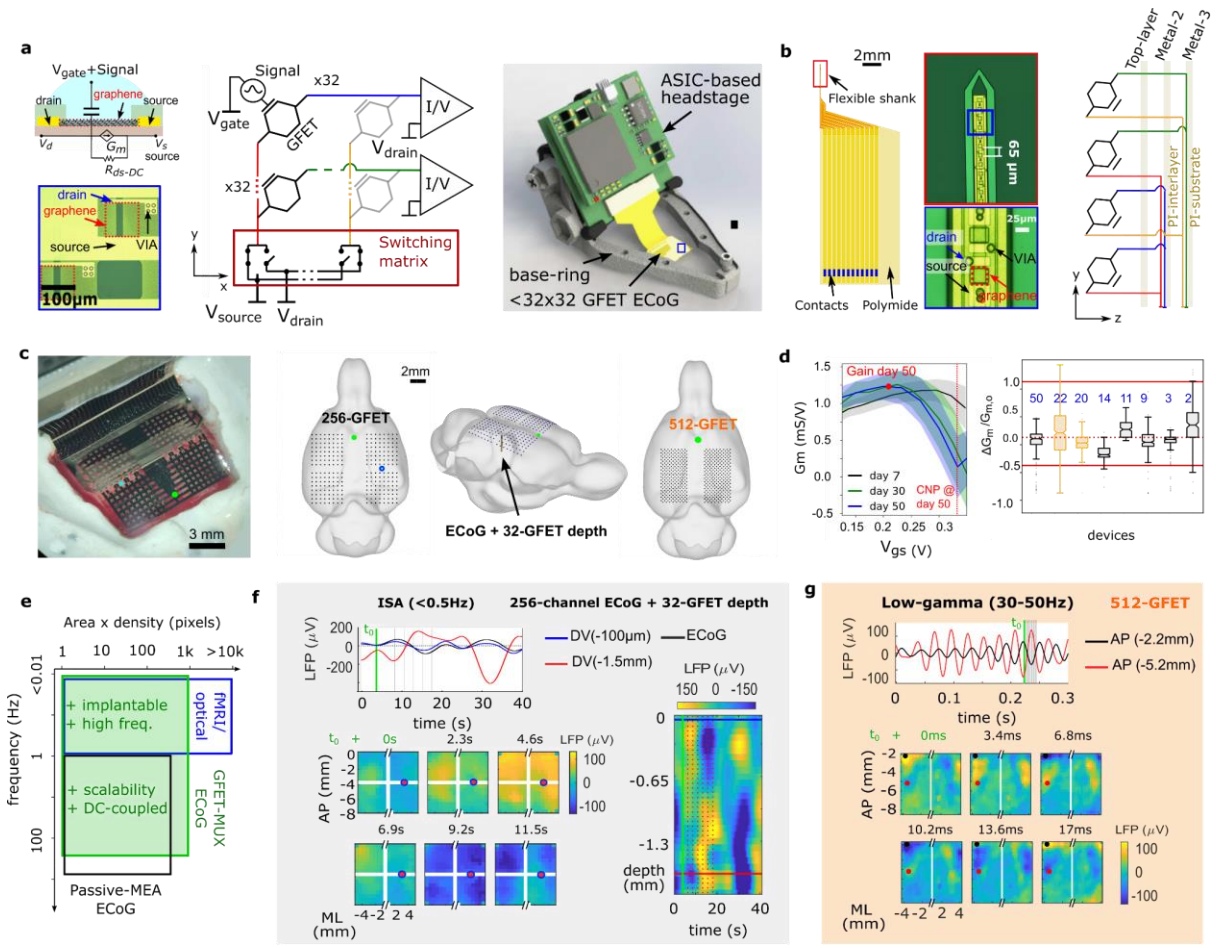

Figure 1| Graphene-based multiplexed large-scale recording technology. a. Schematic of a g-SGFET and its equivalent circuit (top-left). Optical micrography of the graphene transistor array with the position of drain, source, active graphene area and vertical-interconnect-access (VIA) connections indicated (bottom-left). Schematic of a multiplexed g-SGFET array, each hexagon represents a g-SGFET. Rows and columns are connected to the I-V converters and a switching matrix respectively (middle). The headstage and graphene neural probes are shown as assembled on a 3D-printed base ring for implantation (right). **b.** Layout of a 32-channel graphene depth probe (left). Optical micrograph showing the tip of the depth probe (middle). Schematic of a multiplexed g-SGFET array arranged in a linear probe, where multiple metal layers are used to reduce its width (right). **c.** Micrograph of a 256-channel g-SGFET ECoG array implanted over the neocortex of a rat (left) and schematics showing the position of the arrays. Blue dot, the position of the insertion of depth probes; green dot, Bregma (right). **d.** Left: Voltage-dependent transconductance (Gm): median (solid line) and standard deviation (transparent area) for all GFETs in a 256-channel ECoG. Right: the change in Gm from the first day to the last day (in blue) normalised by the Gm on day 1 for all functional GFETs in 256-channel (black) and 512-channel (orange) ECoGs. Red lines, two-fold increase/decrease of Gm. Blue numbers, the number of days implanted for each device (see Extended Data Fig. 3). **e.** Schematic comparison of the spatio-temporal resolution of various imaging techniques. The advantages of multiplexed graphene probes compared to other techniques are indicated in green. **f.** Examples of traces in the infra-slow band (top-left) from representative ECoG and two intracortical channels. Infra-slow voltage maps recorded with a 256-channel ECoG (bottom-left). The white gaps indicate gaps between channel rows/columns (see panel c). The blue circle indicates the insertion point of the depth probe. IsLFP depth profile (right), where the blue and red lines indicate the channels corresponding to the traces on the left panel. **g.** Examples of traces in the low-gamma band (top), and low-gamma voltage maps recorded with a 512-channel ECoG (bottom). White space indicates the gap between hemispheres. The red and black dots indicate the channels corresponding to the two traces on top.

To explore the spatio-temporal dynamics of wide-band LFP during spontaneous behaviour with the improved sensing capabilities of graphene probes, we implanted large-scale ECoGs covering a large fraction of the dorsal neocortex in 8 rats (6 of them with 256-channel and 2 with 512-channel ECoGs, see Fig. 1c, Methods). Additionally, in a subset of animals, surface recordings were combined with multiplexed graphene depth probes implanted into the somatosensory cortex (ML 3.2mm/ AP -3.4mm) through an opening in the ECoG (n=2, see Fig. 1c). Electrophysiological recordings were performed in combination with high-precision 3D motion capture of the rat's head for the classification of behavioural states in recording sessions lasting between 46 min and 248 min (mean of 145.8 min). The chronically implanted neural probes showed stable sensitivity, quantified by transconductance (Gm) of transistors, for up to 50 days (see Fig. 1d and Extended Data Fig. 3). The large-area coverage and high spatio-temporal resolution measurement of the DC-coupled LFP enabled by these devices provided a unique imaging-like electrophysiological window into wide-band brain dynamics (Fig. 1e), as illustrated by the examples of spatio-temporal patterns in the infra-slow and gamma band in Fig. 1f,g and Supplementary Movies 1 and 2.

High-dimensional spatio-spectral characterization of brain states

Similar to how high-density multichannel recordings at micro and mesoscale enable the detection and classification of single units and high-frequency oscillations based on their invariant spatial sources[61], macro-scale recordings could provide an insight into anatomical localization of the sources of the slow oscillatory LFP associated with global brain states. Indeed, the use of multiple channel recordings combined with spectral analysis improves brain state classification[62]. Leveraging on the topographic dense sampling of LFP over the entire dorsal neocortex, and indirectly sampling the dynamics of volume conducted sources localized in the underlying brain areas[63], we hypothesised that the spatial localization of the oscillatory dynamics sources could help with the identification and classification of brain states.

To characterise the variable topography of the oscillatory dynamics associated with distinct brain states, we first computed spectrograms of the LFP and integrated spectral power within various frequency bands for all channels, from delta to low-gamma (Extended Data Fig. 2). These high-dimensional spatio-spectral characteristics of global brain dynamics were then reduced to the first three principal components, which were used for state classification based on a Gaussian mixture model (Fig. 2a). This approach compressed covarying spatio-spectral features and allowed reliable automatic identification of the three major electrophysiological states: slow-wave (SW) state, theta state and high-voltage spindles (HVS)[64–66]. The electrophysiological state segmentation was complemented with the motor state extracted from the 3D tracking data to subdivide behavioral-physiological states into slow-wave sleep (SWS), rapid eye movement (REM) sleep, awake non-theta (Aw. NTHE), awake theta, associated with active movement (THE) and micro-arousals (MA - defined as short bouts of movement during SWS) (Fig. 2b and Methods).

Using the obtained labels of the data segments as ground truth, we tested the separability of data points in the full-dimensional spatio-spectral space without considering the motor information. The separability between state clusters was assessed by embedding spatio-spectral data into a 2-dimensional space using Uniform Manifold Approximation and Projection (UMAP) and computing cluster isolation metric (*L_ratio,* see Methods) in that space (Fig. 2c). The obtained *L_ratio* was then compared to the distribution of *L_ratio* obtained from UMAP-transformed features derived from individual channels treated independently (Fig. 2d). Indeed, separability of labelled states was substantially increased when taking into account spatio-spectral features for the classification, even

leading to effective segregation of states that partially overlap in terms of spatial and spectral content, such as THE and REM. The improvement of cluster isolation metric when using the full dimensional spatio-spectral characteristics compared to only spectral features of independent single channels was consistently present across animals for all the identified states (Fig. 2e, t-test confirms a significant reduction in *L_ratio* across animals and states).

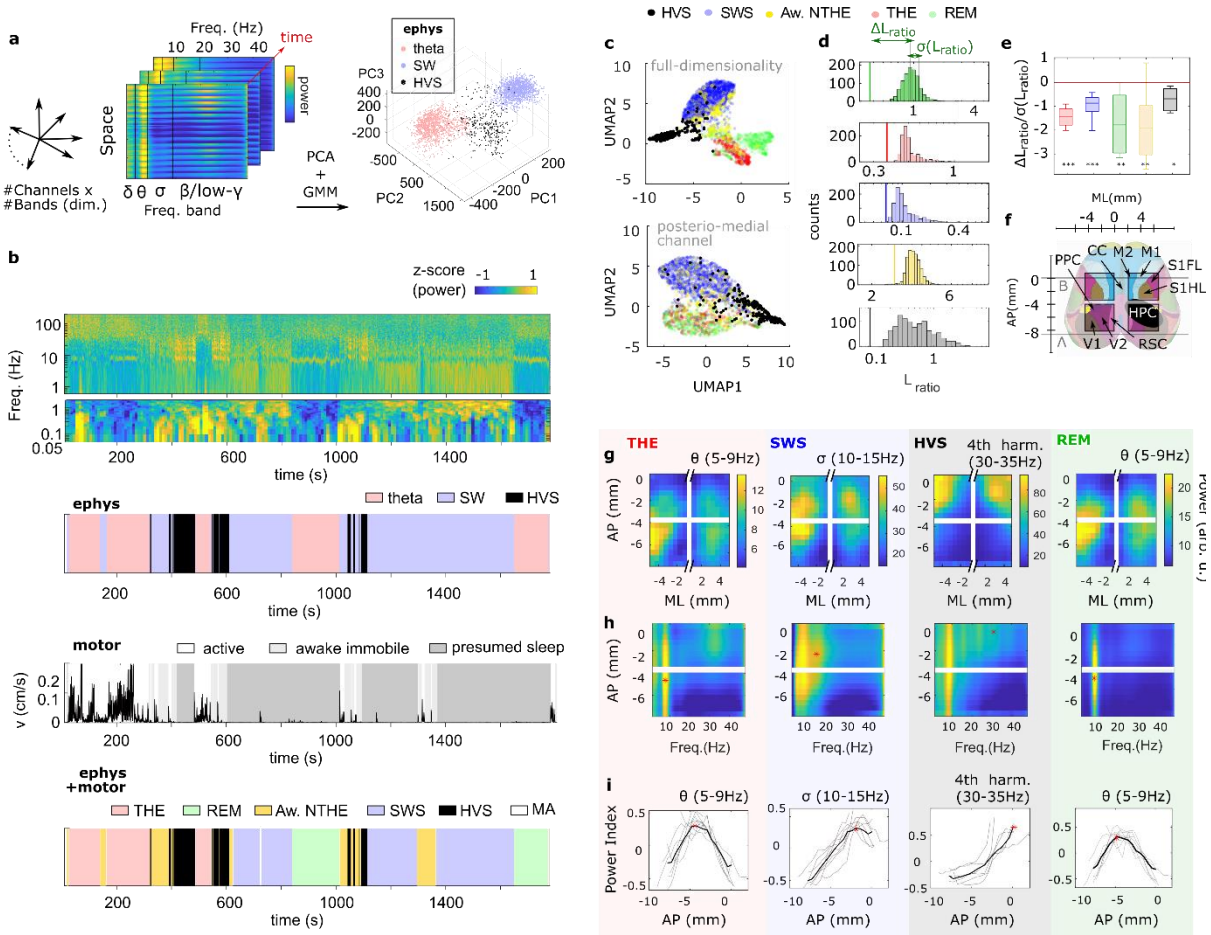

Figure 2| Spatio-spectral characteristics of brain states. a. Representation of the brain state classification procedure. Spectral content in various frequency bands in all channels is used as features for a classifier based on PCA and a GMM. **b.** From top to bottom: Example spectrogram (z-scored) spanning from infra-slow (0.05Hz) to high-gamma (200Hz) bands. Resulting electrophysiological states. The motor state overlapped with the speed of the animal. Combination of the motor state with the electrophysiological state. **c.** UMAP embedding of spatio-spectral characteristics from all channels (top) and from an example posterior channel (bottom). **d.** Distribution of the *Lratio* extracted from individual channels across the array and *Lratio* from full-dimensionality spatio-spectral data (vertical line). **e.** Difference between the *Lratio* from full-dimensionality spatio-spectral data and the median of the *Lratio* distribution across channels (normalized by its standard deviation) (n=8 for THE, SWS and Aw. NTHE; n=6 for REM, n=5 for HVS, one-tailed Wilcoxon signed-rank test p-value: *<0.05, **<0.02, ***<0.01). **f.** Atlas of the rat brain (obtained from EBRAINS database). Projection of the hippocampus on the surface in black. The non-shadowed area represents the sampled area by 256-channel ECoGs. ML, mediolateral; AP, anterio-posterio. **g.** Mean spectral power map within a certain frequency range (top labels) across the array for THE, SWS, HVS, and REM states (from left to right). **h.** Mean ML-axis-average spectrum across the AP axis for THE, SWS, HVS, and REM (from left to right). Spectrum has been re-whitened using an AR model within each state. Red stars, peak in power for the frequency band shown in the g. **i.** Mean ML-axis-average spectral power within a certain frequency band (top labels) across the ML axis, for the THE, SWS, HVS and REM (from left to right). Shaded lines correspond to different animals and the solid line is the mean (n=8 for THE, REM and SWS; n=6 for HVS).

Large-scale and dense mapping of brain activity also enabled the characterization of brain-state-specific spatio-spectral features across cortical regions (Fig. 2f), which contributed to their separability. The mean power maps in space and frequency revealed the spatio-spectral fingerprints of the identified states (Fig. 2g,h), which were consistent across animals (Fig. 2i). Specifically, theta power during THE and REM sleep had a broad peak roughly aligned with the projection of the hippocampus on the cortical surface (see atlas in Fig. 2g for reference). During THE state and REM sleep, the mean power profiles also presented a prominent peak in the low-gamma band (30-40 Hz) in anterior regions, overlaying motor and somatosensory areas (Fig. 2h). During SWS, the power in the delta band was maximal in central-anterior areas, with relatively large variability across animals (Extended Data Fig. 4), while the spindle power was stronger over somatosensory cortices (Fig. 2g-i). Finally, HVSs consistently presented a broadly distributed fundamental (7-10 Hz band) with multiple harmonics with increasingly prominent anterior localization for higher-order harmonics (Fig. 2g-i).

These results suggest that leveraging high-density multichannel recordings over the entire dorsal neocortex can significantly enhance the classification and characterization of the brain states. In the following sections, spatio-spectral characteristics of brain states are used to study the topographical relation between oscillatory dynamics and isLFP.

Spike and wave discharges drive local shifts in the DC extracellular potentials

Having characterised the spatio-spectral characteristics of prominent brain states we next evaluated their spatio-temporal infra-slow correlates across cortical regions. Firstly, we focused on the HVS state, which is a hypersynchronous thalamocortical oscillation that is considered a model of absence epilepsy[65,67] that has all the features of the spike and wave discharge and has been previously linked to spatially inhomogeneous DC shifts[53]. Understanding the relation between this state of hypersynchronous neuronal firing and the DC potential shifts across brain regions and cortical layers could provide clues about the physiological origin of isLFP and guide the discovery of biomarkers for the detection and localization of the epileptic foci[36,68,69]. Specifically, we tested whether and how the topographic structure of the broadband spike-and-wave discharges associated with HVS (Fig. 2g-i) is mapping to the infra-slow spatio-temporal dynamics and performed a detailed investigation of the spatial and laminar profile of the DC shifts associated with this most synchronous endogenously generated thalamocortical oscillatory state.

To characterize the infra-slow correlates of HVS, we analysed the coactivation of infra-slow and spindle-band sources. The duration of HVS episodes showed a long-tailed distribution with a median of 4.7s (Fig. 3a). The HVS events were associated with a striking surface negative DC-potential shift linked to the spike-and-wave activity (Fig. 3a,b), which had a larger amplitude in anterolateral brain areas where the power of spike-and-wave discharges was also larger (Fig. 3c, left and Fig. 2h). Concurrent translaminar recordings from the somatosensory cortex revealed that the DC-potential shift reversed its polarity from negative in superficial layers to positive reaching maximal amplitude in the deep cortical layers (Fig. 3b and c, right). To quantify this observation across all channels, the LFP time-series were filtered into two bands: low-pass below 0.5Hz and band-pass within the 5-30Hz band. Segments of 40 sec centred around the HVS were extracted, concatenated and spatially decomposed in each band via independent component analysis (ICA) to identify spatial maps and temporal dynamics of the main sources for DC-potential shifts and spike-and-wave discharges, respectively (Fig. 3d). The resulting independent components (IC) were sorted based on the mean DC-potential shift around the HVS onset (±2s) to capture both their magnitude and temporal alignment with HVS events (Fig. 3e, f). Inspection of the infra-slow IC1 reconstructed LFP and its spectrogram further illustrates

the correlation between infra-slow dynamics and spike-and-wave discharges for the first IC (Fig. 3f). The mean DC-potential shift dropped quickly for higher ICs, indicating that both energy and temporal dynamics of the wide-band LFP associated with HVS are mostly captured by the first IC component in both frequency bands (Fig. 3g). The activation of IC1 around the HVS onset (and offsets) confirms a consistent topographical DC-potential shift (and return to baseline) associated with the oscillatory dynamics used for HVS detection (Fig. 3h). The loadings of the first IC presented a consistent negative gradient in the posterior to anterior, as well as in the medial to lateral directions (Fig. 3i,j). The depth profile of the HVS showed a phase reversal of the first IC around layer IV for DC-potential shifts as well as for the first band-pass IC of spike-and-wave discharges (see Fig. 3c, j). Overall, these results show that HVS, as hypersynchronous thalamocortical oscillation, generates not only localised spike-and-wave discharges but also a temporally aligned, topographically and trans-laminarly matching DC-potential shift.

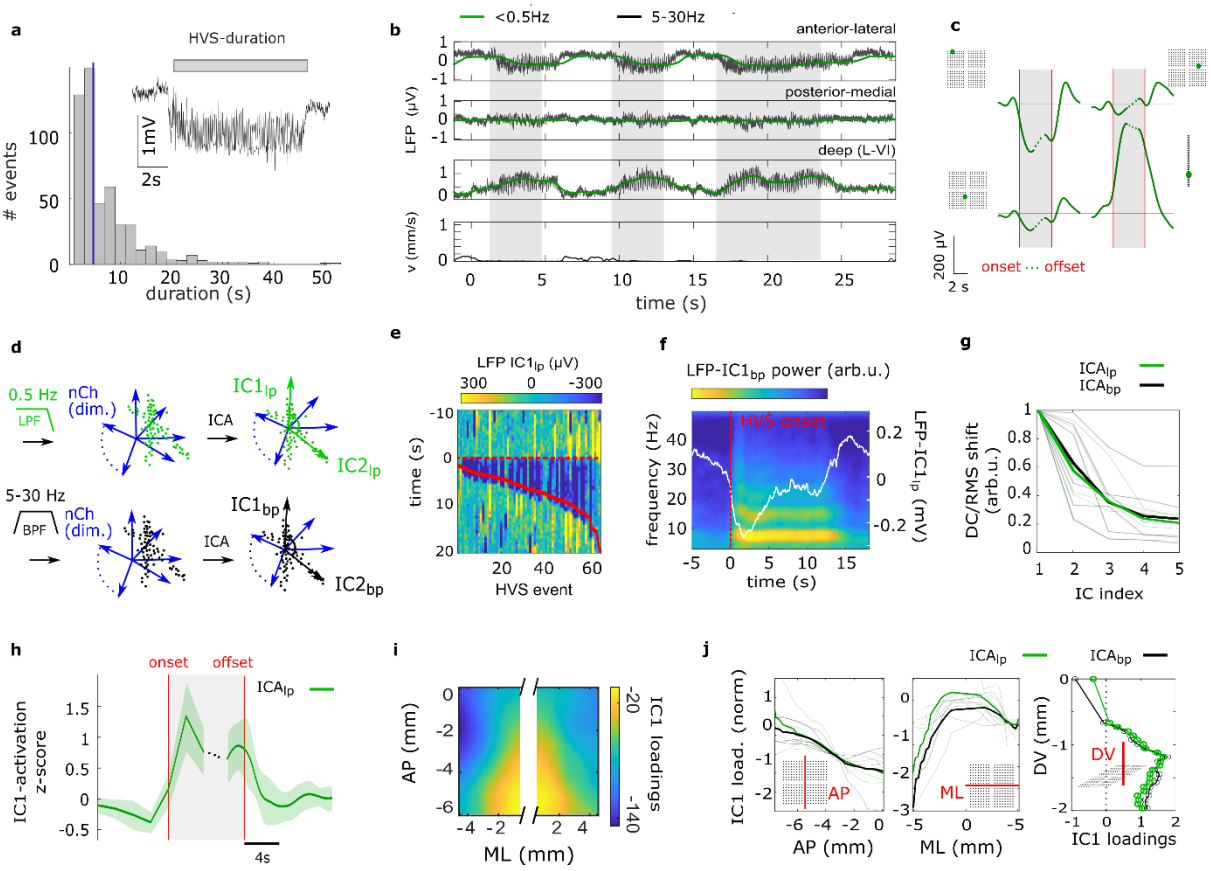

Figure 3| Topographic structure of infra-slow and spike-and-wave sources of high voltage spindles. a. Distribution of HVS duration across animals (median, blue line). Inset, an example of full-band LFP during HVS. **b.** LFP during the occurrence of several HVS events (<30Hz, black and <0.5Hz, green). From top to bottom: LFP for representative anterolateral, posterior-medial and deep channels and speed of the animal. **c.** Mean DC-coupled isLFP around the HVS onset and offset (red vertical lines) for various channels in AP (left) and DV (right) axes in the example animal. **d.** LFP in the infra-slow and 5-30 Hz bands was decomposed by ICA separately. **e.** Colour-coded reconstructed LFP from the $IC1_{lp}$ across HVS events for an example animal. Red lines indicate state onset and offset. **f.** The triggered average spectrogram of the reconstructed LFP from the $IC1_{bp}$ around the HVS onset overlaid with the triggered average of the infra-slow reconstructed LFP for the $IC1_{lp}$ for an example animal). **g.** Mean DC-potential shift around the HVS onset (±2s) for the first five ICs (see Methods, n=6). **h.** Group (n=*6*) average $IC1_{lp}$ activation triggered on the onset and offset of the detected HVS events. Shading is 1 standard deviation. **i.** Median loadings of the first IC (limited to n=4 to show the maximum overlapping area across animals). **j.** Comparison of the first IC loadings across animals (n=6) in the three axes (thick line shows the mean across animals). IC loadings were normalized by their value at -3.5mm w.r.t. Bregma in the AP axis, 4mm w.r.t. the midline in the ML axis and at -1mm w.r.t. the surface for the DV axis.

Infra-slow LFP dynamics mark the transition between arousal levels

We posited that in a similar way that HVS, as an exceptionally synchronous state, is associated with topographically and translaminar structured DC shifts, transitions in and out of the synchronous SWS state would likely be also marked by such infra-slow dynamics. Early reports of state-correlated shifts in DC recordings in animals lack consistency and quantitative topographic and translaminar analysis[27–30]. Recent studies have explored the relationship between the level of arousal and the microstructure of sleep sub-states[70,71,72]. During SWS, the power of sleep spindles varies at the infra-slow time scale, marking cycles in sleep fragility[71] linked to neuromodulatory dynamics[6,7,44,73]. Similarly, neuromodulatory infra-slow dynamics promote the transition into REM sleep[6,7]. Despite this recent progress, the isLFP correlates of these neuromodulatory and thalamocortical synchronisation dynamics, as well as their relation to the microstructure of sleep regulation, remain largely unexplored and limited due to technical limitations[74,75].

To characterize the spatial structure of isLFP associated with SWS states we took advantage of long sleep recording sessions and prior state segmentation (Fig. 4a) and extracted spatial patterns of largest covariance using singular value decomposition (SVD) of the LFP epochs, containing SWS, MA (MA) and REM-sleep and surrounding 10s epochs. While the 1st SV component (SV1) contained a trivial global variation in the signal power captured, the 2nd component SV2 reliably displayed an anteroposterior and mediolateral sign-switching gradient that was topographically consistent across animals (Fig. 4b). Equivalently, isLFP after subtracting the contribution from the SV1 displays prominent transient fluctuations with opposite polarity for anterior and posterior channels, representative extreme poles of this gradient (Fig. 4c).

The troughs in the SV2 score that captured these infra-slow events coincided with the onset of MA and REM epochs, suggesting a correlation between this infra-slow component and the depth of sleep. This observation was confirmed by the cross-correlation between the SV2-score troughs and the MA onsets detected from the motor activity as well as the REM onsets (Fig. 4d). These infra-slow fluctuations recurred with the broad inter-event interval that spanned time scales from 10 to 100 seconds with the median 45.2 ± 4.0 s across animals (Fig. 4e). This is significantly faster than the median intervals between MA detected from motor activity alone, which were of the order of minutes (Fig. 4e). Furthermore, the troughs in the posterior-anterior LFP gradient revealed subtle (subthreshold, <0.5mm/s) micro-movements beyond overt MA with a significant correlation between the integrated micro-movement and the amplitude of the posterior-anterior gradient (Spearman correlation r=0.22, p-value = 0.0017, Extended Data Fig. 5).

The SV2 score around the MA onset showed a consistent transient negative shift and gradual recovery suggesting sequential de-activation and re-activation of a SWS-related topographic DC-potential (Fig. 4f, top left). This pattern was mirrored for the onset of SWS associated with gradual buildup of SV2 score to baseline and abrupt departure from it at the transition into REM sleep, indicating the sequential activation and de-activation of the SWS-related topographic DC-potential captured by the SV2 component (Fig. 4f, top right). Importantly, spindle power dynamics showed a similar gradual onset into the SWS and abrupt offset from it (Fig. 4f, bottom and Extended Data Fig. 6). Analogously to the HVS case, the negative DC shift in anterolateral areas associated with SWS was related to a larger sigma power in anterolateral areas (Fig. 4f). These observations suggest that similar to HVS, SWS state defined by synchronous slow oscillations and sleep spindles is associated with a DC shift with the similar anteroposterior gradient. Hence, in order to interpret the polarity and magnitude of the DC-potential shifts during SWS, the potential has to be referenced to a desynchronised state. Indeed, referencing the LFP (<0.5Hz) to the MA and awake DC level reveals that the shift and associated gradient captured by SV2, namely a negative DC shift reaching, on average, 200 uV in

surface derivations over anterolateral areas during the SWS states (Fig. 4g). Similarly, the translaminar LFP around MA referenced to the aroused state also showed the phase reversal of the DC potential around L-IV with abrupt onset of deep positive shifts of 0.5-1 mV from SWS to MA and gradual recovery into the SWS (Fig. 4h). The topographic structure of the DC shifts in the surface LFP and spindle power showed consistent temporal progression through SWS to MA transitions (Fig. 4i and Extended Data Fig. 6).

Taken together, these results show that the isLFP presents topographical and translaminar dynamics linked to transitions to and from thalamocortical synchronization dynamics of the SWS, which is highly similar to that associated with HVS.

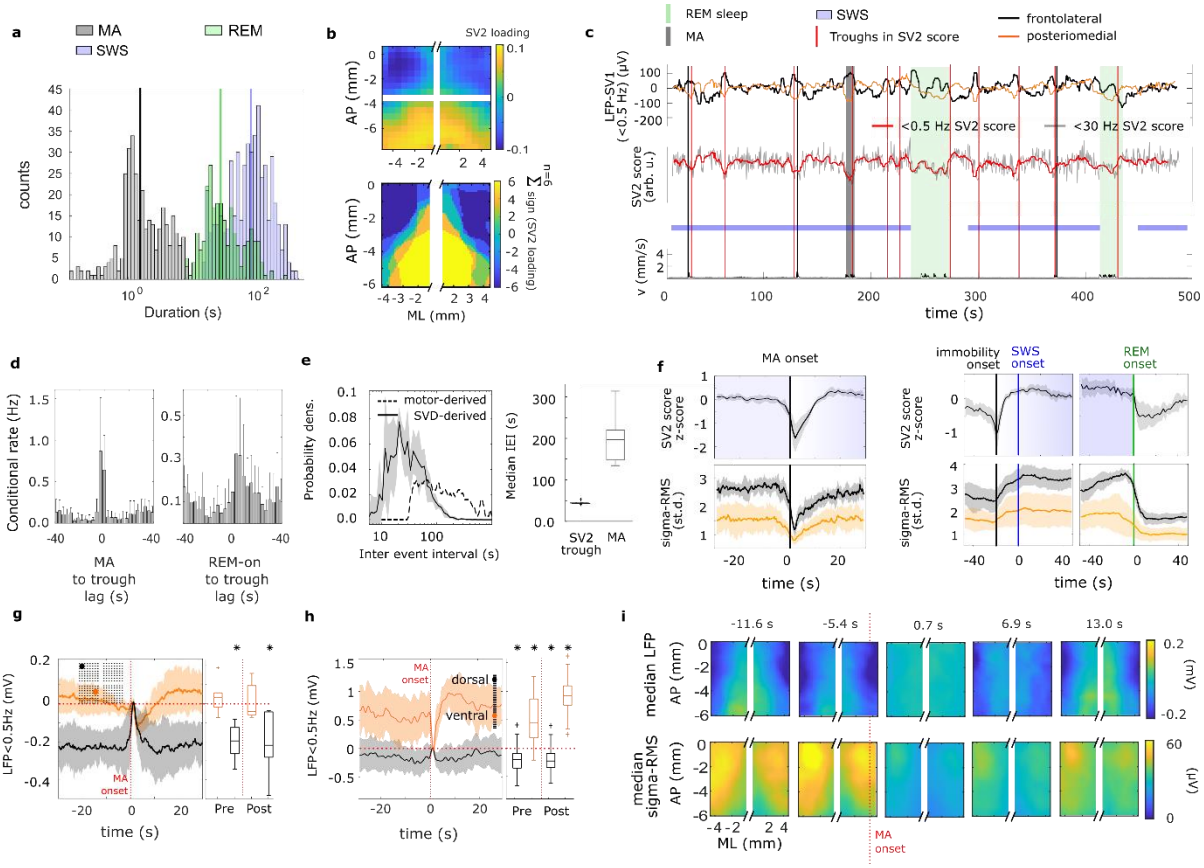

Figure 4| isLFP correlates of sleep state transitions. a. Duration of detected REM sleep, SWS and MA epochs across animals. **b.** Color-coded spatial map of the SV2 loadings for an example animal (top) and spatial map of the cross-animal (n=6) consistency of the SV2 loadings (see Methods, bottom). **c.** From top to bottom: LFP after subtracting the contribution from SV1 for two reference channels, score of the SV2 (<30Hz) and (<0.5Hz), brain states and velocity of the reflective markers on the animal head. Red lines, troughs of SV2 score. **d.** Mean cross-correlogram between state onsets and the SV2 score troughs (standard deviation as error bars, n=6 animals). **e.** Left: distribution of inter-event intervals (IEI) between SV2 score troughs during SWS, mean and standard deviation across animals (n=6) and the IEI distribution between MA accumulated across 6 animals. Right: boxplot of median IEI for SV2 score troughs and MA across animals (n=6 animals). **f.** Top, triggered average of the SV2-score around the MA onset (left) and at the onset of SWS and its transition into REM (right). Bottom, corresponding average normalized spindle power for anterior (black) and posterior (orange) reference channels (n=6, shading is 1 standard deviation). **g.** Triggered average of the isLFP on the MA onset, referenced to the aroused state, for two positions on the surface across animals (left, n=6). The thick lines correspond to the mean and the dashed area to the standard deviation. Insets show reference channel position on the respective arrays. The boxplot shows the distribution of LFP across animals at times -10s and 10s around the MA onset (Wilcoxon signed-rank test $p< 0.05$). **h.** The same as in panel g for one animal and in depth across events (39 events). Superficial channel (DV = -100µm) in black and deep channel (DV = -1.1mm) in orange. Pre and post times in the boxplot correspond to -10s and 10s around the MA onset (Wilcoxon signed-rank test $p< 0.05$). **i.** Median topographic maps of the isLFP rereferenced to MA state (top) and sigma power (bottom) triggered averaged around the SWS-MA transitions (n=6).

Sleep spindles are coupled to global infra-slow and local slow LFP dynamics

The correlation between isLFP and MA suggests that fluctuations in the LFP during SWS could be linked to changes in neuronal synchrony expressed in the amplitude of sleep spindles. This result, together with the topographically matching oscillatory and infra-slow sources during HVS calls for a direct investigation of the topographical coupling between infra-slow and sleep spindles during SWS beyond overt MA. Indeed, sleep spindle power is known to fluctuate at the infra-slow time scale during SWS[71,72]. At the same time, at the finer time scale sleep spindles are organized by the slow oscillation (SO) dynamics[76–78]. To address this question, we first characterized the local generators of sleep spindles and then evaluated their coupling to infra-slow and SO dynamics.

Inspection of the sigma band (10-20Hz) power dynamics reveals topographically structured patterns that presumably reflect the activation of various cortico-thalamic networks involved in the generation of sleep spindles (see Supplementary Movie 3). To characterize the diverse spatio-spectral dynamics in the sigma band, we decomposed the power spectrograms across channels and frequency bins using factor analysis[63] (see Methods and Supplementary Fig. 1). The spatio-spectral structure of the factor loadings reflected diverse oscillatory modes (Fig. 5a) with their respective factor score dynamics displaying transient bouts corresponding to waxing and waning oscillations in the anatomical location and at the frequency reflected by the factor loadings (Fig. 5b). The dynamics of these factors represent a lower-dimensional description of the spatio-temporal variation of sigma power as illustrated in Fig. 5c. Group statistics revealed comparable factors across animals (Fig. 5d and Supplementary Fig. 1) with stereotypical burst durations (0.7±0.2s across animals and factors, Fig. 5e) and harmonic index, a measure of spectral concentration (0.7±0.8, across factors and animals, Fig. 5f and Methods). Spindles in anterior areas (mostly somatosensory and motor cortex, Fig. 5d) present larger amplitude compared to spindles in posterior areas (mostly posterior-parietal and retrosplenial and visual cortex, Fig. 5d) (Fig. 5g, Wilcoxon signed-rank test between the median spindle amplitude across bins in the AP axis and AP coordinates).

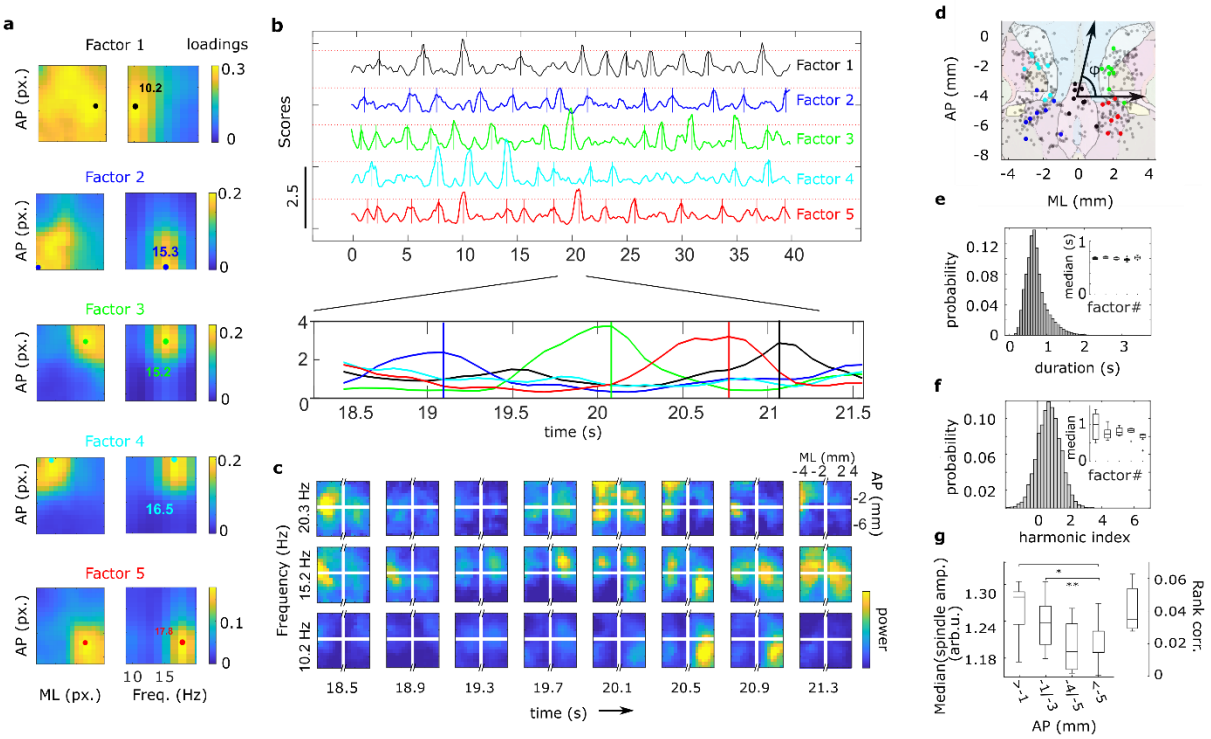

Figure 5| Detection of diverse local sleep spindle generators from the cortical surface. a. Spatio-spectral loadings of the first five factors for an example animal. Filled circles mark the position in space and frequency of the maximum loading. **b.** Score dynamics for the first five factors in panel a. The bottom plot shows overlapping traces in a zoomed-in window. **c.** Example of power dynamics at three different frequencies (rows) across frames (columns) corresponding to time points shown in a. **d.** Position of loadings peak in space (first 30 factors per animal). Coloured dots correspond to matching factors (n= 8 animals). The atlas in the background is the same as in Fig. 2f. **e.** Distribution of half-maximum width of the score peaks across the first five example factors. The inset describes the median of sleep spindle duration (in seconds) for all matched factors across animals (n=8 animals). **f.** Harmonic index distribution across factors for an example animal. The inset shows the median of the harmonic index for each of the matched factors across animals (n=8 animals). **g.** Median spindle power for all factors localized across the AP axis (n = 8 animals). Wilcoxon signed-rank test, * p-val=0.031, ** p-val=0.016. The right-axis shows the rank correlation between amplitude of spindles and the AP-position of their maximum loading across animals.

Having characterized the transient oscillatory modes of sleep spindles, we sought to identify the sources that underlie the temporal dynamics of their occurrence. As microarousal states were associated with topographic and translaminar isLFP fluctuations (Fig. 4c, d), we investigated whether these fluctuations in the LFP exhibit similar spatial profiles away from the MA and if they correlate with the occurrence of sleep spindles within the SWS state. Indeed, isLFP during SWS presented oscillations that were characterized by the same topographic pattern across the AL and PM regions (Fig. 6a,b and Supplementary Movie 4) and the phase reversal around cortical L-IV (Fig. 6a and 6c) as DC shifts associated with transitions into and from the synchronous HVS and SWS states. These spatial patterns of synchronous states thus were recapitulated in the microstructure of SWS synchrony reflected by the isLFP dynamics suggesting a common generating mechanism. We detected the troughs in the isLFP in the anterolateral region of interest (-4.2mm, -1.5mm / ML, AP), linked to larger DC-potential changes during SWS (Fig. 4g), and computed their cross-correlation with the occurrence of sleep spindles in different locations (anterior-left/right and posterior-left/right). Independent of their spatial localization, sleep spindles were consistently locked to the surface-negative phase of the infra-slow oscillation (Fig.6d and 6e). The fact that infra-slow fluctuations globally modulate local sleep spindles suggests that, although the detected spindle generators are orthogonal and present a low degree of overlap at a faster time scale (Fig. 5b,d), their rate is strongly correlated at the infra-slow

time scale (Extended Data Fig. 7). In turn, the level of global synchrony of the SWS state, reflected by the spindle rate, is strongly coupled to infra-slow dynamics marked by the topographic and depth-reversing LFP patterns.

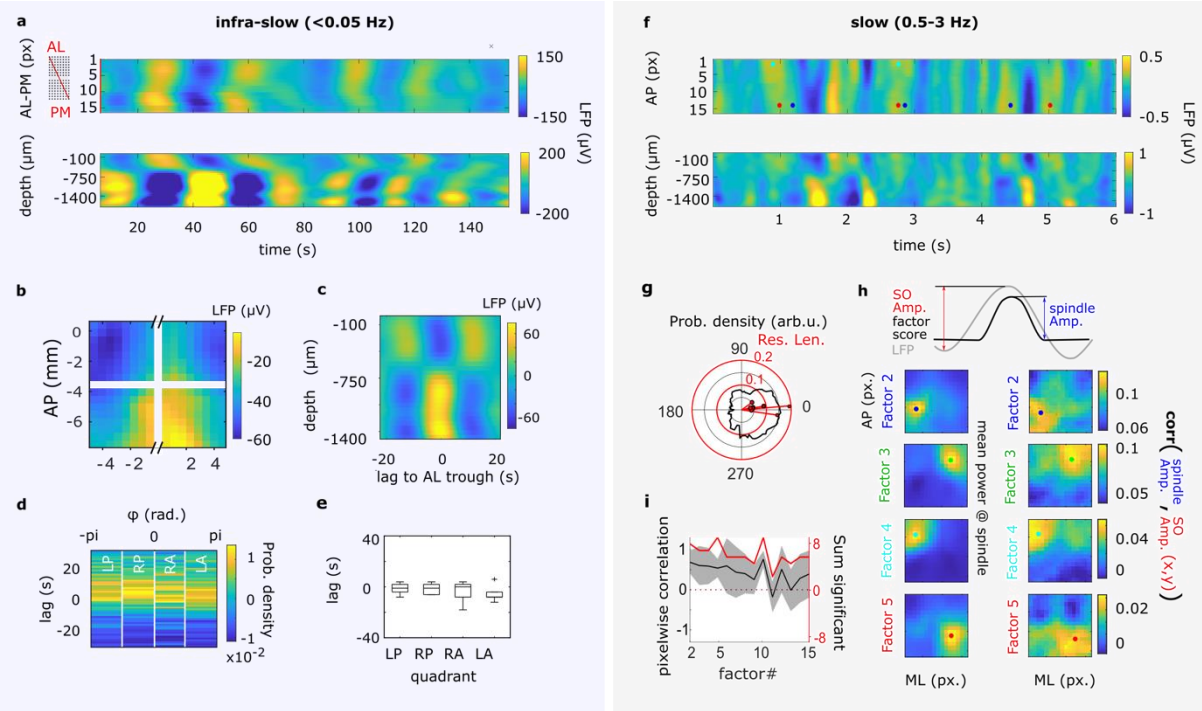

Figure 6| Coupling between infra-slow and slow LFP and local sleep spindles. a. Example of the isLFP in the AL to PM axis (top) and simultaneous recording across cortical layers (bottom). **b.** Mean isLFP (<0.05 Hz) triggered at the trough in AL channels. **c.** Mean infra-slow (<0.05 Hz) LFP profile across cortical layers. **d.** Cross-correlogram between the troughs in the AL isLFP (<0.05 Hz) and time of occurrence of spindles detected in different quadrants. **d.** The time lag of maximal cross-correlation across animals and ECoG quadrants (no significant differences observed between different quadrants, paired-sample t-test). **f.** An example of the LFP in the 0.5 - 3 Hz band for the 16 channels in the fourth column of the ECoG array from the left hemisphere (top) during SWS. The coloured dots correspond to the time stamps for the spindles detected with factors 1 to 5 represented in Fig 5b and 5d. The simultaneously recorded isLFP is shown below. **g.** In black, the distribution of the phase of SO at the time of a spindle accumulated across animals (n=8) and factors 1–10 sorted by variance. In red, the resultant vector for the phase of SO at the time of spindles for factors 1-10 is shown for all 8 animals separately with dots. **h.** Left: mean spindle band power at the spindle time points for an example animal for factors 2 to 5 (same as in Fig. 5c and 5d). Right: the topographical representation of the correlation between the amplitude of the SO cycle and the UP-locked spindle amplitude for factors 2 to 5 (same as in Fig. 5c and 5d). **i.** The similarity between the spindle power maps and the SO-spindle correlation maps measured as correlation between the maps in the two columns of panel h at the hemisphere of maximum loading. The mean and standard deviation of this topographical correlation across animals is shown for the first 15 factors sorted by variance. The right axis shows the sum of significantly correlated factors across animals for the first 15 factors (permutation test p<0.05, 1000 permutations).

Thalamocortical sleep spindles are well-known to be modulated by the SO as they are induced by cortico-thalamic excitation provided by the UP-states[76]. We, therefore, investigated whether the coupling between the SO dynamics in the LFP and sleep spindles could present topographical specificity that was lacking at the infra-slow time scale. Inspection of the raw signal suggests the well-known coupling between global oscillations, with a phase reversal around L-IV, and sleep spindles. Moreover, a second-order topographical modulation became apparent from the raw data (Fig. 6f). To quantify this observation, we computed the phase distribution for global SO at the spindles time, which confirmed the occurrence of spindles at the peak (positive polarity) of the global surface slow waves, i.e. UP-state of the SO[79] (fig. 6g). Global slow negative waves, known as delta waves, detected

on the surface were paralleled with a depth pattern that had a phase reversal around L-IV linked to SO DOWN-states[80] (see Supplementary Fig. 2). Following the validation of the temporal coupling between SO and sleep spindles, we investigated the topographical relation between the amplitude of SO and the amplitude of sleep spindles. The local trough-to-peak amplitude, i.e the difference between LFP values at the time of the preceding delta wave and concurrent positive wave in each pixel across the array, representing the local magnitude of the SO cycle showed a stronger correlation at the location of spindles (Fig. 6h, i). This coupling was also significant for the preceding trough and the concurrent positive wave separately, but weaker for the trough following spindles (see Extended Data Fig. 8). These results reveal that the magnitude of local DOWN-UP-state transitions, representing a local SO dynamics, biases both the timing and the amplitude of the local sleep spindle oscillations occurring during the UP-state.

Discussion

Multiplexed graphene micro-ECoGs to investigate large-scale oscillatory and infra-slow dynamics

Here, we demonstrate the development and application of graphene-based active neural probes for reliable recordings of large-scale, high-density and wide-band epicortical and intra-cortical LFP in freely moving rats. Previous advances in flexible micro-ECoG arrays enabled increased sampling densities across large cortical areas[47–51]. However, the complexity of connectors and front-end electronics in non-multiplexed arrays constrained the scalability and miniaturization of recording systems[49,50]. On the other hand, systems based on high channel-count multiplexed flexible arrays have so far lacked the technological maturity for their application in chronic settings in freely moving animals[46]. The presented technology enables the brain-wide electrophysiological equivalent of imaging of the LFP from DC to higher frequencies at high sampling rates and thanks to the flexibility and miniature electronics allows recordings during unconstrained behaviour. This combination of technical capabilities represents a unique window into the mesoscale synchronization across the brain across spatio-temporal scales revealed by the brain-wide broad-band LFP signals.

Leveraging these technical advancements we dissected the relation between synchronous brain states derived from spatio-spectral features of the LFP and the infra-slow dynamics derived from spatio-temporal and translaminar patterns of the isLFP. Although the biophysical origin of isLFP is unclear and might involve multiple mechanisms[33,28,69,3], the relationship we observed between synchronous brain states and infra-slow isLFP across brain regions narrows down the possible sources. The dynamics we identified in the isLFP is consistent with that observed in numerous studies using different readouts that reflect fluctuations of synchrony, including in derivatives of hemodynamics such as the blood-oxygenation-level-dependent (BOLD) signal[81,82], infra-slow fluctuations of ACh, NE and 5HT[6,7,73], fluctuations of power of oscillatory dynamics[8,15,71] and spiking of single neurons[11]. Our findings suggest that the isLFP could arise from infra-slow changes in extracellular ionic concentration gradients driven by the synchronous activity of large neuronal populations, and shaped by metabolic and neuromodulatory factors.

Large-scale spatio-spectral brain state segmentation and characterization

We identified synchronous brain states in an unsupervised manner based on dimensionality reduction of the topographic maps of the LFP spectra. While the conventional approach relied on specific LFP spectral patterns derived from a single electrode capturing state-specific oscillatory signals

via volume-conduction from cortical and hippocampal sources[63,83,84], the use of distributed intracortical derivations has proven beneficial for more accurate state identification[62]. Indeed, brain state-specific dynamics emerge in distributed large-scale networks shaped by neuromodulatory systems[85,86]. Associated state-specific oscillatory dynamics synchronize neuronal populations across different spatio-temporal scales in both cortical and subcortical regions giving rise to multiple spectrally distinct and spatially distributed sources[24] that are reflected via volume-conduction in the LFP across the brain. The spatio-spectral pattern of the LFP across the brain provides most the accurate information for state detection and classiciation[87]. In analogy with sorting of the extracellular action potentials, this requires large-scale, dense, recordings capable of identifying cross-scale dynamics and localizing volume-conducted sources[25,61]. Topographical localization of the spectral content associated with distinct spectral features of different brain states allowed for the improvement in state segmentation compared to the conventional approach using one or few channels, which often yields a continuum between states[83,84]. This approach could have a further implication for clinical vigilance to account for spectral non-stationarity of the brain dynamics associated with sleep sub-states such as local sleep[78,88,89], alternation of tonic and phasic REM[8,90–92] and NREM or cycling alternating pattern of NREM sleep[93] , which link to a complex sleep microstructure associated with fluctuations of the level of arousal[94].

Furthermore, distinct state-specific topographic patterns help to characterize and further study underlying network dynamics including thalamocortical originated slow waves[78], sleep spindles[88,95–98] and limbic theta oscillation[99]. Future work should dissect the current sources and generators contributing to complex topographic spectral features associated with each state. The unsupervised approach for the state classification might also reduce the bias in the state detection. Interestingly, both awake and to a lesser degree REM sleep states were associated with frontal beta oscillations that were consistent with that reported in sensory-motor areas in awake animals and humans[100,101]. Alternatively, this frontal gamma represents olfactory-reafferent gamma oscillation that is prominent in the awake state compared to sleep[102,103].

We anticipate that a combination of the source localization and unmixing of oscillatory components based on their spectral and phase information would allow the decomposing of conventionally homogenous brain states into substates and identify their contributing non-stationary components. While theta dynamics appears homogenous, there are multiple anatomically distinct current generators that are contributing to theta band in the LFP across the rodent brain, including multiple generators in the hippocampus and medial entorhinal cortex[104,105] that are partially independent. These diverse generators give rise to travelling waves across ventro-dorsal extent[106,107] as well as to independent hippocampal type 2 theta generator[108], and sources generated by hippocampal projections to the medial prefrontal cortex[63,109] and retrosplenial cortex, to name a few. In addition, breathing induced re-afferent components of the LFP would contribute to the LFP and overlap with neural oscillations frequency bands[103,110].

The spatial structure of the HVS reported here is consistent with earlier work in older rats[53,111], but allowed for more sensitive topography-based detection and classification of less synchronous oscillations characteristic for the younger age used here[67]. In addition to oscillatory features, topographic and laminar patterns of synchrony-associated infra-slow transients provide a guideline for their optimal detection in animals and pave the way for a translation to the clinic for seizure localization[112,69]. Multi-channel recording systems, combined with stimulation electrode grids and control theory strategies[113], could enable precise control of the dynamical state of large-scale

556 networks, potentially down to transient oscillatory states such as HVS or sleep spindle oscillatory
557 bursts.

558 Anatomically invariant spatial features of the LFP spectrum could become particularly
559 important for state characterization in the face of large inter-subject variability of the underlying
560 oscillation frequency and expression level. Furthermore, spatio-spectral features of the EEG enable
561 predicting individual psychiatric phenotype[114]. The detailed characterization of spatio-spectral
562 features of brain states opens new avenues for therapeutical interventions. Previous studies have
563 shown that electrical stimulation can influence brain regions across both local and long-range
564 connections[113,115,116], creating large-scale network effects observable in the LFP[115]. Our findings
565 support the design of closed-loop electrical stimulation therapies locked to large-scale infra-slow brain
566 dynamics[117]. Identification of field potential sources in the infra-slow frequency band opens the door
567 to the discovery of novel biomarkers for the detection and localization of pathological states, such as
568 epileptic seizures, migraine or stroke[28,69,112,118–120]. Furthermore, detection based on infra-slow
569 features could be advantageous for chronic neural implants where a reduction of the sampling rate
570 implies a reduction in power consumption and required processing power as well as required
571 bandwidth for data logging or wireless transmission, with potential implications for seizure localization
572 and prediction[121].

573 *Topographic characterization of sleep spindles and their coupling with local slow waves*

574 Spatially localized and spectrally distinct sleep spindle detection that benefits from dense
575 large-scale recordings as demonstrated here can be considered a natural finer-scale extension of the
576 brain state classification. Regional diversity of sleep spindle frequencies has been reported in humans
577 and rodents[95,122,123,98,124–127], likely reflecting distinct thalamocortical networks. Our results represent
578 an unbiased characterization of spatial and frequency localized sleep spindle oscillations that are
579 consistent with and extend prior work. Sleep spindles with slower (10 Hz) frequency tended to be
580 more global, while the majority of spindles had a widely varying frequency covering sigma to beta
581 range and were topographically localized. The fact that spatio-spectral localization provides a more
582 sensitive and unbiased analysis of the transient oscillations is analogous to high-frequency oscillations,
583 which enables the dissection of precise temporal dynamics of distinct circuit motifs and their
584 functional investigation[63,128,129].

585 Alternating Down/UP-state dynamics of the slow oscillation (SO) and sleep spindles have been
586 functionally implicated in hippocampo-cortical communication[78,130] supporting systems memory
587 consolidation[131,132]. The precise detection and localization of sleep spindles and UP/DOWN-states
588 could provide further insights into the mechanism by which these dynamics facilitate memory
589 consolidation in distinct cortical areas. These mechanisms have been proposed[130] to rely on the fine-
590 time scale coordination of hippocampal sharp wave-ripples (SPW/R) by sleep spindles that have been
591 shown for those detected in parietal[130] and prefrontal cortices[133]. Data in humans suggests that this
592 coupling is stronger for parietal spindles that lag anterior ones[123,134] likely reflecting anteroposterior
593 propagation of the locally generated UP-states that recruit sleep spindles[4,78,79,89,132,135]. High-density
594 recording allowed us to perform bilateral, large-scale and high-density mapping of both slow waves
595 and sleep spindles and assess their local interaction further refining this complex dynamic blueprint.
596 The antero-posterior gradient of synchronization reflected in the isLFP topography was associated
597 with the higher power of sleep spindles as well as slow waves, consistent with a more likely origin of
598 K-complexes in and their propagation from the frontal regions[135]. Furthermore, while global SO
599 dynamics entrains sleep spindles independent of their localization[136], the amplitude of the local

Down/UP-state-associated slow wave correlates with the amplitude of the spatially aligned local sleep spindles. This is consistent with local DOWN-UP-state recruitment of localized spindles giving rise to a local K-complex[77] and may reflect local packets of memory consolidation that might be differentially coupled with SPW/R[137,138].

Qualitative model of the relation between neuronal synchrony and DC-potential shifts

The biophysical source of infra-slow field potentials remains unclear, with some works suggesting a non-neuronal origin[3,28]. Our characterization of synchronous oscillatory network dynamics and isLFP across cortical regions and layers provides new insights into the origin of infra-slow changes in the extracellular potential.

We identified a unified relationship between the topography and cross-laminar profile of the isLFP and oscillatory power across diverse synchronous states, ranging from the high-voltage spindle state, SWS state or fluctuations within SWS. Both spike-and-wave discharge component of HVS and the associated DC shift had topographically identical sources centred on somatosensory areas (Fig. 7a, left and Fig. 3i,j). The topography of DC shifts associated with SWS state flanked by MA and REM sleep states, as well as infra-slow fluctuations in the LFP and the spindle power within SWS, had a similar gradient from anterolateral to posterior-medial areas (Fig. 7a, right and Fig. 4, 5) matching the topography of sleep spindle power (Fig. 7a and Fig. 2g, 4h, 5g). Furthermore, in every synchronous state, the translaminar depth profile of the DC-coupled LFP matched that of the associated slow waves. HVS-associated translaminar DC profile had a phase reversal around layer IV, similar to that of spike-and-wave discharge[139] (Fig. 7b, left and Fig. 3). Similarly, infra-slow fluctuations during SWS and around the SWS/micro-arousal transitions showed a similar phase reversal around layer IV, which is comparable to the phase reversal of delta waves[140,130] (Fig. 7b, right).

To explain these convergent observations, we propose a qualitative physiological model that unifies them and provides a mechanism by which neuronal synchrony gives rise to the translaminar DC-potential generator in all these states. What is common for all synchronous dynamics, is that during the active phase, the spike phase of the HVS or the UP-state of the slow oscillation, synchronous neural firing results in an increase of intracellular Ca^{2+} concentration[141,142]. This leads to the activation of multiple K^+ currents, most prominently, calcium-dependent potassium (I_{K-Ca}), as well as ATP-dependent K^+ and inward-rectifier K^+ currents, that are responsible for the termination of the active state, repolarization of the membrane potential and an increase in extracellular potassium concentration ($[K^+]_o$)[143–148,142,149–152](Fig. 7c). These activity-dependent hyperpolarizing currents are larger in layer V where there is higher recurrent excitation and firing rate[153–155] giving rise to higher net current density of I_{K-Ca} and a localized current source in this layer during the DOWN-state associated delta wave[130,156] or HVS wave[139] (Fig. 7d), and, respectively, layer V dominated accumulation of $[K^+]_o$. During the wave phase of HVS or the DOWN-state, the extracellular potassium ions are buffered by glia[58] and pumped back into the cell by NaK-ATPase pump[157]. However, under repeated activation of K^+ conductance during synchronous activity these mechanisms are not sufficient to return the $[K^+]_o$ to baseline level, resulting in a build-up of $[K^+]_o$ [57,158–161] leading to a state-dependent concentration gradient $\Delta[K^+]_o$ (Fig. 7e,f)[57,58,160], with a sustained layer 5-dominance[57,160] (Fig. 7g) matching the delta/HVS wave profile (Fig 7b) that originated this gradient. Here, we propose that this sustained $[K^+]_o$ gradient during states of high synchrony will lead to the generation of sustained electrical dipole by activating the electrogenic NaK-ATPase pump and, correspondingly, an outward current with amplitude dependent on a translaminar concentration[157,161,162] (Fig. 7g, h). In this manner, the sustained and deep layer localized concentration

gradient of $[K^+]_o$ would be a consequence of neuronal synchrony giving rise to a similar depth-reversing DC dipole as that of the delta/HVS wave (Fig. 7h). Importantly, the mechanism we propose here is independent of the source of synchrony, and is consistent with numerous prior work showing that both electrical stimulation of the neocortex or spontaneous and induced seizures results in both $[K^+]_o$ accumulation with matching translaminar gradient as well as translaminar reversal of the extracellular DC potential from negative at the surface to positive in deep layers[28,33,40,57,158–160,163].

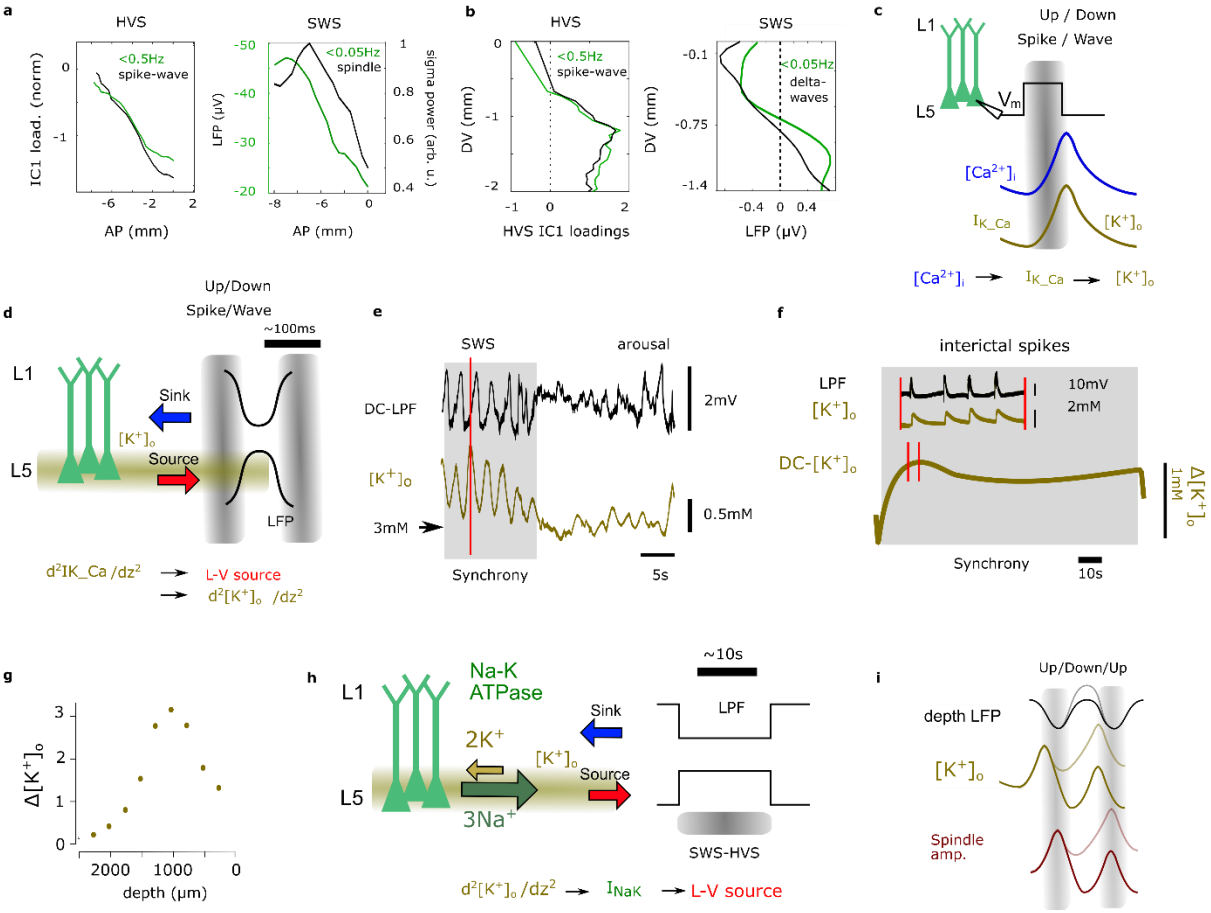

Figure 7| Qualitative model of the link between synchronous states and DC-potential changes. a. Topographical relation between the amplitude of spike-and-wave discharges and their infra-slow correlates (left) and between the power of sleep spindles during SWS and mean isLFP at the AL troughs (right). **b.** Translaminar profile of the HVS spike-and-wave amplitude (left) and its infra-slow correlates (right). **c.** Synchronous states such as UP-states and the spike component of HVS drive an increase in intracellular calcium, which leads to the opening of K^+ channels that hyperpolarize the neurons. **d.** The increase in K^+ conductance during the UP-DOWN-state transition is larger in layers with high neuronal activity, leading to an LFP source around L-V and generation of a K^+ gradient around this layer. **e.** Empirical evidence for the relation between extracellular potassium concentration and slow oscillations as well as its DC level change between SWS and desynchronized states (adapted with permission from Seigneur et. al. 2006[58]). **f.** Experimental data showing the buildup of $[K^+]_o$ during an induced trace of interictal spikes (adapted with permission from Moody et. al. 1976[57]). **g.** Depth profile of the amplitude of this buildup (adapted with permission from Moody et. al. 1976[57]). **e.** The buildup of a change in the layer-specific DC-level of potassium leads to a layer-specific activation of the electrogenic Na-K pump, which in turn generates a DC LFP source. **f. g.** Schematic of the relation between the amplitude of slow oscillations, potentially generated by changes in the potassium conductance during the DOWN-state and the accumulation of potassium in subsequent cycles leading to increased excitability and sleep spindle amplitude.

674 Activation of the outward current driven by the NaK-ATPase pump at the same time, could
675 causally influence the network dynamics by increasing the resting potential of neurons and contribute
676 to terminating a synchronous state[161]. This causality could be reflected on the finer timescale in the
677 relation between the larger amplitude of delta waves associated with a larger increase in $[K^+]_o$ and
678 higher excitability during the following UP-state as reflected in the amplitude of sleep spindles (Fig.
679 7i).
680
681 *Spatial topography of the infra-slow LFP*
682
683 A characteristic topographic pattern of the synchrony-associated isLFP fluctuations is potentially
684 homologous to a larger power of 0.1 Hz infra-slow dynamics in sensory-motor regions observed in
685 human EEG[164]. The origin of this topographic pattern is not well understood, though a number of
686 studies converge on the topographically overlapping networks identified from coherent dynamics of
687 different observables and in different species. First, fMRI dynamics reveal several poorly correlated
688 networks, including sensory-motor and posterior-medial attentional and default mode networks[165],
689 with limited correlation to isLFP reported[166,167]. State-associated juxtaposition of anterolateral and
690 posterior-medial networks have been observed in infra-slow neural activity using various imaging
691 approaches in mice[21,168,43,169,170]. Importantly, a recent study using Ca^{2+} imaging in mice identified
692 topographically-matching areas as REM-opponent (sensory-motor) and REM-like (retrosplenial-
693 visual), with the latter stronger activating during REM sleep and MA. Interestingly, sensory-motor
694 areas receive the lowest density of cholinergic innervation[170], which might enable higher levels of
695 synchronization in this region during neuromodulatory dips within NREM sleep. While offline
696 dynamics has been often ascribed to activation of the default mode network (DNM), which includes
697 posterior-medial regions and hippocampal formation, our results do not trivially align with DNM
698 boundaries. First, while we observe higher power of sleep spindles in sensory-motor regions, they co-
699 occur at the same infra-slow phase across the brain. Second, infra-slow neuromodulatory dynamics
700 co-modulate brain-wide synchrony, including hippocampal and cortical synchronous activity[18,44,171]. As
701 a result, hippocampal SPW/R covary with cortical slow oscillations and spindle power on the infra-
702 slow timescale[172–174] . On top of this co-variation, hippocampal projections to frontal and retrosplenial
703 cortices perturb bistable slow oscillation dynamics contributing to the observed topographic patterns
704 measured using Ca^{2+} and voltage imaging[43,138,137], giving rise to complex and poorly interpretable
705 topographic patterns across the neocortex[175,43,137,176].
706
707 In addition, we propose that the anatomico-biophysical origin of the surface LFP might also contribute
708 to the observed topography. According to our proposed model, infra-slow negative potential is
709 generated by deep positive and surface negative infra-slow dipoles (Fig. 7h) distributed across the
710 whole cortical mantle. However, as medial cortical regions fold 90 degrees toward the midline and
711 posterior regions fold towards the cerebellum, infra-slow dipoles in these regions rotate 90 degrees
712 as well, resulting in volume conduction of deep sources to the overlaying cortical areas and
713 attenuating the effective amplitude of the infra-slow surface LFP through destructive
714 interference[25,177].
715
716 *Relation between infra-slow potentials, the sleep microstructure and neuromodulatory activity*
717
718 Previous studies have shown the relation between neuromodulatory dynamics during SWS
719 and in the SWS-REM transition[144,70–72,44,6,73,7,171] and fluctuations in the sleep spindles occurrence,
720 which covary at the infra-slow time scale of 0.01-0.05Hz, often referred to as ultra-slow[83].
721 Furthermore, both synchronous states such as slow wave and HVS are similarly suppressed by the

722 cholinergic tone[178], highlighting that the topographically structured isLFP readout we uncovered can
723 be a sensitive biomarker of the synchronous state devoid of neuromodulatory activation. Indeed, we
724 show that isLFP dynamics can also uncover states of increased arousal level reflected in extremely
725 subtle (<0.5mm/s) movements during SWS, consistent with the relation of neuromodulatory dynamics
726 to overt and covert MA[6,171].
727
728 Recently, neuromodulatory dynamics and brain state alternation have been shown to be bi-
729 directionally causally interrelated to both systemic and local $[K^+]_o$[179,180]. High neuromodulatory
730 levels are associated with elevated $[K^+]_o$, while it tonically decreases during NREM sleep and
731 immobility, setting up the backdrop for a strong driving force of outward K^+ necessary for effective
732 negative feedback for any synchronous slow dynamics, as well as allowing for larger translaminar
733 gradients of $[K^+]_o$ giving rise to infra-slow potentials.
734
735 While our proposed model for the isLFP requires experimental validation, it has clear predictions.
736 Specifically, it predicts that the active current generator is associated with synchronous states and
737 thus disambiguates the polarity of the DC signal that remained elusive so far[33,29,28,69]. Indeed, DC-
738 coupled recordings pose a challenge in the interpretation of the signal polarity and identification of
739 the active phase of the oscillation in the case of periodic dynamic[181,177], given the lack of a stable
740 absolute potential reference. Based on our model of active DC-potential shifts generation by sustained
741 translaminar $[K^+]_o$, we argue that referencing the DC-potential to the desynchronized states (i.e. MA
742 and REM) in contrast to SWS results in accurate characterization of the topographical changes and
743 interpretable DC signal. In contrast, conventional high-pass filters aimed to remove slow accumulating
744 DC artifacts would result in effective "zeroing" of the long-lasting SWS-related DC potential and
745 generation of false and opposite polarity transients around short-living active states.
746
747 *Relation between isLFP and vascular dynamics.*
748
749 Infra-slow dynamics that our observations reveal parallels the same timescale hemo- and
750 vasomotor dynamics, which is prominent in all species, depends on both central circuits, autonomous
751 nervous system and blood vascular resonance[182,165,183,184]. These dynamics have been shown to be
752 coherent with EEG/LFP in the infra-slow band and modulate the occurrence of synchronous oscillatory
753 states in animals and humans[185,186,167,187,188]. How exactly the infra-slow dynamics observed in the
754 neural activity and hemo-/vasomotor dynamics are causally related remains a matter of debate
755 [183,8,189,3,190]. It appears that the most parsimonious explanation of the plethora of infra-slow dynamics
756 of the same frequency (ca 0.1 Hz) at different levels is a bi-directional interaction of multiple networks:
757 neural, astrocytic, vascular that rely on interactions of different types and timescales including
758 neuromodulatory, metabolic, which would give rise synchronization around common resonant
759 frequency at rest condition.
760 While infra-slow rhythm rhythmogenesis is a complex global phenomenon, infra-slow
761 vasomotor dynamics might contribute to the observed isLFP. Both neural activity-independent[189,190],
762 neuromodulation driven[191], as well as synchronous neural activity-driven[3,190] hemo-/vasomotor
763 dynamics, can give rise to electrical potential changes. Blood vessels present a potential shift with
764 respect to the extracellular space, leading to possible extracellular infra-slow potential variations
765 caused by vasomotor dynamics[3] that would be measurable across the brain. However, isLFP patterns
766 associated with synchronous states are not consistent with those expected from the state-related
767 vasomotor dynamics. Firstly, MA and REM present opposite vasomotor dynamics at the transition
768 from SWS[192–194] inconsistent with comparable spatiotemporal isLFP around these two state
769 transitions. Secondly, the translaminar phase reversal in the isLFP reported here and elsewhere[28,40]

770 cannot be explained by potentials induced by vasomotor dynamics. Interestingly, increased $[K^+]_o$
771 could modulate vasomotor activity by the inward-rectifying channels in the blood vessels[3], but this
772 effect is unlikely to be laminar-restricted to give rise to phase-reversal of the isLFP. Rather than
773 vasomotor dynamics dominating the generation of extracellular infra-slow potentials, our model
774 supports that the laminar-specific changes in $[K^+]_o$ that generate sustained dipoles could also
775 contribute to the delayed vasomotor dynamics. This could be the mechanism linking topographic
776 infra-slow potentials measured by fb-EEG and resting state networks from the BOLD signal[45].
777

778 *Conclusion*

779 Large-scale, DC-coupled LFP recordings enabled by multiplexed graphene neural probes
780 provided insights into the topographical and translaminar relation between neuronal synchrony and
781 isLFP dynamics. These results expand our understanding of cross-frequency coupling across brain
782 regions and states, providing new insights into the mechanisms of cortical excitability and sleep
783 regulation. Altogether, this work highlights the potential of infra-slow isLFP features as sensitive
784 biomarkers, with promising applications in both clinical and fundamental neuroscience.

785

786 **Methods**

787 **Graphene probes microfabrication**

788 Large-scale graphene neural probes were fabricated on a 4" wafer following the procedure
789 described before[55] with minor modifications. An initial 4µm-thick polyimide (PI-2611, HD
790 MicroSystems) was spun-coated on a Si/SiO_2 4" wafer and baked at 350°C. Polyimide was chosen as a
791 substrate due to its stability and biocompatibility[51,60,195,196]. A first metal layer 30nm Ti for adhesion,
792 300nm Au for conductance and 10nm Ni as diffusion barrier at high temperatures) was deposited by
793 electron-beam vapour on a previously photodefined negative AZ 5412E (Clariant, Germany) and then
794 structured by a lift-off process. Then, a 2µm-thick polyimide interlayer was deposited to separate
795 metal layers and vertical interconnection access (VIA) holes opened using a 200nm-thick Al mask (by
796 lift-off using AZ 5412E, and etching by O_2 plasma. Afterwards, the graphene grown by chemical vapour
797 deposition on Cu was transferred (process done by Graphenea). Graphene was patterned by oxygen
798 plasma (50 sccm, 300W for 1min) in a reactive ion etching (RIE). The photodefinable resist used to
799 protect the graphene in the channel region was HIPR 6512. After the graphene etching, a second metal
800 layer was patterned on the contacts following the same procedure as for the first layer, but this time
801 performing an ozone cleaning treatment before metal deposition in order to improve the contact
802 resistance and noise[197]. Subsequently, the transistors were insulated with a 3-µm-thick
803 photodefinable SU-8 epoxy photoresist (SU-8 2005 Microchem), keeping uncovered the active area of
804 the transistors channel. SU-8 is known to limit the stability of devices in physiological conditions to a
805 semi-chronic time scale[198,199]. Finally, the polyimide substrate was structured in a reactive ion etching
806 process using a thick AZ9260 positive photoresist (Clariant) layer as an etching mask. The neural
807 probes were then peeled off from the wafer and placed in a zero insertion force (ZIF) connector to be
808 interfaced with our custom electronic instrumentation.

809

810 **Recording systems design**

811 We used two recordings systems based on two different design approaches; the first is based on an
812 application specific integrated circuit (ASIC)[54] and the second on commercially available discrete
813 components[56]. The ASIC-based approach enables the integration of the system in a fully implantable

814 headstage and optimizes the operation for higher channel count graphene probes, while the system
815 based on discrete-components relaxes spatial constrains on the design and facilitates early adoption
816 of the technology. To cope with the large dynamic range of the DC-coupled signals, including the
817 variability in the DC current offsets between graphene transistors, both design approaches present a
818 low gain (10x) transimpedance amplifier as the first amplification. To reduce the dynamic range of the
819 signal, the ASIC-based system includes current offset cancellation circuitry with a programmable
820 resistor array to subtract current at the transimpedance amplifier input corresponding to specific g-
821 SGFET offsets (Extended Data Fig. 1). The amplifier voltage noise at the output increases with the
822 number of columns (Extended Data Fig. 2). In order to minimize the contribution of e_{amp}, the ASIC
823 implements a correlated double sample (CDS), which samples the noise from the amplifier and
824 subtracts it from the sampled signal. On the other hand, the system based on discrete components
825 copes with the large dynamic range of the signal by digitizing it at two stages of amplification (Fig. S1b-
826 left). The output from the first stage is digitised after the low gain transimpedance amplifier as the
827 DC-coupled signal. The analog signal after the first stage is high-pass filtered above 0.1Hz to eliminate
828 common offsets and further amplified before digitization resulting in the effective prevention of
829 quantization noise.

830 After amplification, the ASIC implements the analog-to-digital conversion (ADC) and the serialization
831 for effective data transmission. The TDM read-out integrated circuits (ROIC) have been combined with
832 an electrophysiology recording platform from Multi Channel Systems (MCS). The setup is based on an
833 interface board (IFB) and a signal collector unit (SCU) (Extended Data Fig. 1). The IFB provides a USB
834 3.0 interface with the computer, while the SCU provides a bridge between the field-programmable
835 gate array (FPGA) on the headstage (built around the LFE5U-45F device from Lattice Semiconductor)
836 and the IFB itself. On the other side, a custom made cable ends in an 8-pin polarised connector PZN-
837 08-AA from Omnetics Connector, and carries the 4 differential wire pairs needed for the master-slave
838 data input and output, clock and supply to the headstage. The headstage is composed of two PCB
839 modules, the ROIC carrier and the FPGA board, which is capable of managing several ROIC modules.
840 The FPGA already contains several IPs and all the necessary blocks for the ROIC application, such as
841 the 51.2 MHz phase-locked loop (PLL), a mapped block random access memory (BRAM) module, the
842 high-frequency serializer/deserializer (SerDes) and the low-voltage differential signalling (LVDS)
843 drivers for the system cable. The complete hardware setup is configured with the help of the open-
844 source Scientific Python environment and a proprietary dynamic-link library (DLL) from MCS. The
845 system based on discrete components is based on the conduction of the analog signals (as changes in
846 the drain-to-source current) via 32 wires to a NI-DAQ card for digitisation and communication with
847 the PC.

848

849 **Ethical approval and animal handling.**

850 The experiments in-vivo were in accordance with the European Union guidelines on the protection of
851 vertebrates used for experimentation (Directive 2010/63/EU of the European Parliament and of the
852 Council of 22 September 2010). Electrophysiological experiments with Long Evans rats were carried
853 out under the German Law for Protection of Animals (TierSchG) and were approved by the local
854 authorities (ROB-55.2-2532.Vet_02-22-22). Rats were kept under standard conditions (room
855 temperature 22 ± 2 °C, 12:12 h light–dark cycle, lights on at 10:00), with food and water available ad
856 libitum.

857 **Surgical implantation of large-scale graphene ECoGs**

858 A cohort of 8 Long Evans rats, weighing between 558±121 g were used for this study. As previously
859 described[53], anaesthesia was induced with Midazolam (2mg/kg), Medetomidin (0.15mg/kg) and

860 Fentanyl (0.005mg/kg). After 1h of surgery, isoflurane at a concentration of 0.5-1.5% was provided
861 while monitoring vital signs. The posterior-dorsal area of the head was shaved, the skin was locally
862 disinfected with Povidone-iodine and subcutaneously infiltrated with the local anaesthetic
863 Bupivacaine. The skin was then incised and the dorsal skull was cleaned carefully by blunt dissection
864 and the temporal muscle was separated from the skull. The skull was cleaned with H_2O_2 (3%) and
865 phosphoric acid (KERR - Gel Etchant, 37% phosphoric acid), sequentially for a few seconds and then
866 by scratching the surface with a scalpel. A 3D printed base ring made of Polylactic acid (tough PLA,
867 Ultimaker) was anchored to the skull with at least six screws in the frontal side of the skull, two more
868 on each temporal plate of the skull, two on the occipital plate and with Metabond cement (Parkell).

869 After at least 7 days of recovery, the animals underwent a second surgery for the implantation of the
870 neural probes. This two-step surgery ensured fast recovery following the probes

871 implantation. The animals underwent the same anaesthetization procedure described above, with
872 Metamizol (110mg/kg) provided in order to maintain the analgesic effect 4h after the start of the
873 surgery. A small craniotomy (~1mm x 2mm) was opened above the cerebellum for the placement of
874 an Ag/AgCl reference electrode (100µm thick) close to the cerebellar surface. In order to minimize the
875 contact of Ag with the tissue and improve the electrochemical stability of the reference, the electrodes
876 and the cerebellar surface were covered with a drop of agar solution (0.5%). Secondly, a large
877 craniotomy was opened on the frame defined by the base-ring with a width of 1.1cm and length of
878 1.3cm. In order to perform such a large craniotomy, the skull was removed in five pieces. Four
879 symmetric quadrants and the skull on the midline. For the detachment of the skull from the dura, a
880 blunt tool was used, with special care on the area around the sinus. Afterwards, the dura was removed
881 within the area of the craniotomy and the device was placed in its final position. The craniotomies
882 were covered with prepolymeri[sed PDMS (~100µm thick – same composition as above) and sealed
883 with Vetbond (Animal Care Products, USA). A 3D-printed skull replacement was then lowered using
884 the stereotaxic Microdrive until the PDMS surface and slightly compressed by ~200µm to correct the
885 brain bulging and fixed in place with optical cement. The cranial window was filled with dura-gel
886 (Cambridge Neurotech) in order to seal the cable of the probe.

887 **Implantation of flexible depth probes.**

888 For the insertion of flexible depth probes, rigid silicon shuttles with polyethylene glycol (PEG)
889 10000MW were used as previously reported[60,200]. Flexible depth probes were aligned with the silicon
890 shuttles with previously added PEG using a micromanipulator under the microscope. When properly
891 aligned, the PEG was molten on a hot plate. In order to have finer control of the placement of the
892 connectors during implantation, the shuttle was attached to an additional motorised stage on the
893 stereotaxic frame. After insertion of the depth probe into its final location, the PEG was dissolved using
894 physiological saline solution. Once the flexible probe was delaminated from the shuttle, it was
895 immobilised using a thin layer of agar (0.5% mass) after cooling down (shortly before solidifying).
896 Subsequently, the additional motorised stage was used to extract the shuttle without moving the
897 flexible probe or its connector. Finally, the probe was fully immobilised using optical cement (Evoflow
898 - Ivoclar Vivadent, Liechtenstein) and the connector moved to its final position using the stereotaxic
899 frame.

900 **Electrophysiological recordings**

901 Electrophysiological recordings using the large-scale graphene probes and depth graphene probes
902 were carried out in a circular open field arena (0.8m in diameter) with high walls transparent to IR
903 light for motion capture tracking. The recordings lasted between 46 minutes and 248 minutes (mean

of 145.8 minutes). The discrete electronics system was based on a previous version[56], upscaled to enable the operation of up to 256 channels. Shortly, the system consists of a commercial data acquisition card (National Instruments DAQ-Card, USB-6363), and a custom-built amplification front-end and switching array for multiplexing (see Extended Data Fig. 1). The sampling frequency of the DAQ-Card of 1MHz is shared among the 256 channels, the DC-coupled and AC-coupled amplification stages. For each switch between columns 2 samples are dropped for signal stabilization leading to a sampling frequency of 651Hz each channel. This system was operated using the code published in the repository (https://github.com/RamonCortadella/LargeScale-WideBand/) for the acquisition of calibration $I_{ds} - V_{gs}$ curves as well as for brain mapping. In the second system, an ASIC[54] implements the switching matrix, I-V conversion with offset cancellation and further amplification and digitization with a correlated double sampling. An FPGA on the headstage implements the digital communication between the ASIC and an interface board (IFB, Multi-Channel Systems and MCS-SCU-in-vitro, Multi Channel Systems) to implement the data transmission to the headstage. The system was operated using customised software from Multi-Channel Systems. The sampling frequency was 12 kHz per channel, way above the LFP band, to reduce high-frequency noise (see Extended Data Fig. 2).

Signal pre-processing

The acquired signals representing the drain-source currents through all transistors in the active matrix were calibrated using the stationary transfer curve ($I_{ds} - V_{gs}$) by interpolating the DC-coupled current. Using this method, variations in the G_m due to V_{gs} drifts are corrected[201]. Following interpolation, the signals were high-pass filtered using a median filter with a time constant of 200s, which preserves better changes in the abrupt changes in the DC-potential level compared to IIR filters. The signals were converted to a binary format (16-bit) with a range of 10mV for full-band recordings (ASIC-based system), 30mV for DC-coupled channels (discrete-components-based system) and 3mV for the AC-coupled channels (discrete-components-based system). Bad channels were then detected as outliers (x330 or /330 times the power) in the low frequency (1-10Hz) or high frequency (60-120Hz) within neighbouring 3x3 pixels. The bad channels were then interpolated using the "scatterinterpolant" function in Matlab, and was median-filtered with a 3x3 kernel and using constant padding.

Data analysis

Spectrogram calculation

Spectrograms were computed using the multitaper method on the whitened signal. Whitening was performed using a first order autoregressive model[202] fitted on the LFP in the 1-100Hz band (excluding the 50Hz and 100Hz pick-up noise peaks by a notch filter). The window length for the FFT was 2.36s (or 2.46s for the 512 channel probes). The overlap between FFT windows was half of the FFT window duration and time-frequency bandwidth NW was 3, corresponding to 1.27Hz frequency bandwidth. The spectrograms for factor analysis of sleep spindle power were computed with a window of 1.576s, 7/8 window overlap, NW=2, frequency bandwidth of 1.27 Hz.

Brain states classification

Brain state classification was based on the combination of behavioural states obtained from motion tracking and electrophysiological states obtained from the high channel-count neural probes (see Results section). Motor state classification was based on thresholding the speed magnitude (with a speed of 5mm/s) to define periods of activity and inactivity (>5s) and motor-defined "sleep" starting after 20s of inactivity and lasting at least 20s more). The time series of transitions between the electrophysiological states (i.e. SWS, theta and HVS) classified from spectral characteristics were smoothed using median filter to eliminate exceedingly fast transitions. SWS and theta states were filtered with a time constant of 20 s and HVS states with a time constant of 1.5s. Then, the electrophysiological states were combined with the motor state for complete brain state classification. SWS was defined as overlapping periods of sleep and SW activity. Awake non-theta (Aw. NTHE) states were non-sleep periods overlapping with SWS state. THE (exploratory state) is comprised of overlapping theta and active state. For REM sleep classification, the active/inactive state transition time series was median filtered with a time constant of 20s to exclude brief movements during REM and preserve the continuity of the state. Electrophysiological states classified as theta that were overlapping with presumed sleep states were classified as REM when preceded by SWS. HVS events were defined solely based on the electrophysiological classification. Finally, MA were defined as bouts of active state shorter than 10s within 40s of inactivity and limited to SWS (with these short bouts of movement not interrupting the SWS epochs).

Measurement of separation between state clusters

Quantification of the separability of brain states was evaluated using rescaled Mahalanobis distances. More precisely, the Mahalanobis distances for all data points with respect to the points in a particular state were computed. Then, the Mahalanobis distances of all points that do not belong to that particular state were rescaled and summed. The rescaling was performed according to the complementary of the cumulative chi-squared distribution with 2 degrees of freedom (number of dimensions in UMAP embedding). Using this rescaling, those points that are nearer to the cluster of the particular state, but do not belong to it, have a higher contribution. The summed distance divided by N is the *L-ratio* used to quantity the separability of clusters resulting from the automatic spike-sorting, a procedure analogous to state-sorting implemented here[203]. The larger the *L-ratio*, the less isolated is the given cluster.

Computation of mean spectrum across cortical regions and states

The mean spectrum was computed from the spectrogram across samples for each brain state to provide spatio-spectral characteristics of each state. The mean spectrum was re-whitened in each state separately by performing a linear detrend on the log-transformed mean spectrum. The linear fit from a single reference channel (second row and second column) was used for all channels. The log-transformation was reversed by raising the values to the exponent and the integrated power within various bands was computed. Note that rewhitening highlights spectral features while maintaining the topographical information unaltered. However, it rescales the power scale and as a result the power is expressed in arbitrary units. To compare the integrated power in different frequency bands across states and animals, the median power in the AP axis was computed, mean-subtracted and normalised by its range (maximum minus minimum integrated power).

Independent component analysis of wide-band LFP around HVS

LFP was band-pass filtered in the infra-slow part via low-pass filtered below 0.5Hz and the oscillatory part capturing power in of the spike and wave activity by filtering in the 5-30Hz band. Epochs of

988 multichannel time series for these two bands centered around the onset of HVS (±20s) were
989 detrended, their median subtracted, concatenated and ICA (FastICA[204]

990) was applied to the resulting time series giving rise to two sets of independent components (ICs), IC_{lp}
991 and IC_{bp}. The activation dynamics of all ICs were used to reconstruct the contribution to the LFP from
992 each component by multiplying the maximum loading value and its activation score. To sort the ICs,
993 the mean reconstructed LFP (and RMS) at the site of largest loading was computed for the 2s time
994 window preceding and following the HVS onset. The DC-potential shift and RMS was used for sorting
995 the ICs in the infra-slow and spike and wave activity bands respectively. The loadings of the first
996 component were compared across animals after normalizing the loadings by their value at the channel
997 located -3.5mm with respect to bregma (AP axis) and 3.5 with respect to the midline (ML axis).

998 *SVD of infra-slow LPF and analysis of temporal relation to state transitions*

999 The LFP during SWS and REM plus the preceding and following the 20s was concatenated across
1000 sessions for each animal, filtered below 0.5Hz and rank transformed to normalize and reduce the
1001 impact of motion artefacts on the decomposition. The SVD of the transformed signal revealed the
1002 common second component (SV2) across animals with consistent anteroposterior and mediolateral
1003 gradient. A consistency of the 2nd SV component loadings across all animals was quantified by summing
1004 up the sign of the left-singular vectors across all animals, which would give +/-6 if the loading has a
1005 consistent sign across all animals (see Fig.4b bottom). Infra-slow events characterized by this
1006 component were detected as troughs in the SV2 score timeseries with the prominence above 90th
1007 percentile. These events were used to compute the inter-even intervals and cross-correlation with the
1008 MA.

1009 *Triggered average of isLFP and spindle power around states onset*

1010 To compute the triggered average, the LFP was low-pass filtered below 0.5Hz and the signal within
1011 the MA (0.7s post onset) or REM sleep (10s post-onset) was subtracted in the time window of interest
1012 (±30s for MA and ±150s for SWS/REM onset).

1013 *Identification of putative down-states for depth probe position estimation*

1014 The LFP signal during SWS from ECoG recordings was filtered in the delta band (0.5-3Hz) and the mean
1015 across all channels was used to detect global delta waves. Delta waves were detected as large
1016 amplitude troughs (>2 x standard deviations). This procedure was validated using concurrent depth
1017 recordings where delta waves consistently presented a phase reversal across layers (see
1018 Supplementary Fig. 2), in accordance with prior literature[78].

1019 *Factor analysis for topographic sleep spindle detection*

1020 Factor analysis was performed as previously described[63]. Briefly, it consists of the following steps. First,
1021 the power per frequency bin and channel is log-transformed to bring the distributions closer to
1022 symmetric (normal) and then z-scored to have homogeneous variance across all dimensions. The
1023 spectrogram is also spatially smoothed in each frequency bin and time point using a 3x3 median filter
1024 across pixels. Then principal component analysis is performed and 99.9% of the variance is kept. Factor
1025 orthogonal rotation was then performed using the Varimax method[205], using the simplicity criteria to
1026 obtain a matrix of factor loadings. The simplicity criterion finds directions with the most parsimonious
1027 structure in the covariance matrix, which have high loadings in only a few spatio-spectral variables
1028 and close to zero in most of them. In addition, factor loadings are all positive which eliminates the
1029 ambiguity in the polarity of principal components.

Specificity calculation

The spectrogram in the sigma band was spatially smoothed (using a 3x3 median filter across pixels) for each frequency bin and time point. Then the spatial-frequency coordinates with a loading above half of the maximum were taken as the signal and those below as the noise. The ratio between the mean power of the signal and the mean power of noise was defined as the specificity of a factor to describe the covariance structure of the spectrogram in the sigma band.

Sleep spindle duration estimation

The duration of sleep spindles was computed from the activation dynamics of distinct factors. The activation, analogous to ICA activations or PCA scores, reflects the projection of the log-transformed, z-scored spectrogram on the direction of the loadings. This projection does not reflect a measure of reconstructed power but of log-transformed, z-scored power. The log transformation was reversed, effectively stretching positive deviations, and the duration was defined as the full width at half maximum (FWHM) of the activation peaks. The traces shown in Fig. 5b correspond to the activations after reversing the log transformation.

Matching of factor loadings

For comparison of factor characteristics across animals, factor loadings from different animals are matched based on their Euclidian distance in a 7-dimensional feature space. The features used for matching are the sign in the ML axis, the sign in the AP axis with respect to the centre of the array, the actual position in the array in units of pixels (X and Y axis), maximum frequency in rescaled frequency axis (centred at 0 and normalised by the maximum variation of 5Hz). The number of channels with loadings above half of the maximum loading and the number of frequency bins with maximum loading above half of the maximum (both normalised by the number of channels in a quadrant of the grid) were also used.

Harmonic index calculation

The spectrogram was log-transformed and z-scored to be in the same space used for factor rotation. Then its value was taken at all sleep spindle occurrence times (i.e. times of peaks in the activation of individual factors) at the location and at the frequency of peak of the respective factor loadings. The power at the peak frequency minus the mean of the ±5Hz points defines our measure of harmonicity. The harmonic index can be interpreted as the number of standard deviations between the power at the frequency of maximum loading and the power at 5Hz below and above (in the z-scored and log-scaled power space).

Temporal coupling between infra-slow networks activation and sleep spindles

The time difference between each of the spindle events from all factors and the troughs in the isLFP in an AL region of interest (-4.2mm, -1.5mm / ML, AP) were computed. Then, the JPDF for lags and the location of the spindle oscillator (defined as the quadrant with maximum loading using polar coordinates centred on the midline and at - 4mm from Bregma in the AP axis) was computed. The same distribution was computed from randomised time points within SWS periods for the gradient peaks and the JPDF recomputed from 10 randomizations. The mean JPDF from the randomised distributions was subtracted from the non-randomised JPDF in order to eliminate the edge bias produced by having gradient peaks close to the onset or offset of SWS epochs.

Coupling between slow oscillations and local sleep spindles

To evaluate the coupling between SO and sleep spindles we first evaluated the phase statistics of global SO at the time of peaks in scores of the first 10 factors for all animals by taking the phase of the mean LFP signal across the entire array. To show the preferred phase and strength of modulation for all animals separately we computed the resultant vector for the first 10 factors independently on each of the 8 animals. Once the temporal coupling was established, we looked into topographical coupling between SO and sleep spindles by calculating the correlation between the amplitude of the SO in all channels of the array and the amplitude of sleep spindles for each of the first 15 factors and each of the 8 animals. The amplitude of the slow oscillation was determined by finding the preceding trough (between 0.8 and 0.2s of the spindle time) and the peak (within 200ms of the spindle time) at the location of maximum loading. The SO amplitude at these times was computed for all channels and their correlation to the spindle score amplitude was calculated.

Statistical methods

Mean or medians are given with standard deviation. Significance testing of deviations from zero was done by the Wilcoxon signed-rank test. The statistical significance of the positive and negative deviations from zero observed in the triggered average was assessed by a permutation test for each pixel and time point. The sigma power median across events was compared by the Wilcoxon rank-sum test to the shuffled distribution across all frames and pixels. To take into account the false discovery for such a large number of comparisons we applied the Benjamin and Hochberg correction both for the LFP deviations from zero and sigma power deviations from the shuffled distribution[206]. To evaluate the topographical coupling between sleep spindles and SO the correlation maps and the factor loadings were compared by computing the correlation between these two maps in the hemisphere of maximum loading. To check for the significance of the correlation, the pixels in the correlation map were shuffled and a p-value for the correlation was obtained (1000 permutations).

Data availability

The characterization of devices in-vitro and the complete electrophysiological and motor tracking dataset is available from the corresponding author upon request. Movies can be found in (https://doi.org/10.12751/g-node.kv2mlt).

Code availability

The complete code for analysis of electrophysiological data is available from the corresponding author upon request. Code for the operation of the custom-built recording system can be found in https://github.com/RamonCortadella/LargeScale-WideBand/

References

1. Buzsáki, G. & Draguhn, A. Neuronal Oscillations in Cortical Networks. *Science* **304**, 1926–1929 (2004).

2. Palva, S. & Palva, J. M. Discovering oscillatory interaction networks with M/EEG: challenges and breakthroughs. *Trends Cogn. Sci.* **16**, 219–230 (2012).

3. Drew, P. J., Mateo, C., Turner, K. L., Yu, X. & Kleinfeld, D. Ultra-slow Oscillations in fMRI and Resting-State Connectivity: Neuronal and Vascular Contributions and Technical Confounds. *Neuron* **107**, 782–804 (2020).
4. Alfonsa, H. *et al.* Intracellular chloride regulation mediates local sleep pressure in the cortex. *Nat. Neurosci.* **26**, 64–78 (2023).
5. Krishnan, G. P., González, O. C. & Bazhenov, M. Origin of slow spontaneous resting-state neuronal fluctuations in brain networks. *Proc. Natl. Acad. Sci.* **115**, 6858 (2018).
6. Kjaerby, C. *et al.* Memory-enhancing properties of sleep depend on the oscillatory amplitude of norepinephrine. *Nat. Neurosci.* **25**, 1059–1070 (2022).
7. Zhang, Y. *et al.* Interaction of acetylcholine and oxytocin neuromodulation in the hippocampus. *Neuron* **112**, 1862-1875.e5 (2024).
8. Watson, B. O. Cognitive and Physiologic Impacts of the Infra-slow Oscillation. *Front. Syst. Neurosci.* **12**, (2018).
9. Palva, J. M. & Palva, S. Infra-slow fluctuations in electrophysiological recordings, blood-oxygenation-level-dependent signals, and psychophysical time series. *NeuroImage* **62**, 2201–2211 (2012).
10. Väyrynen, T. *et al.* Infra-slow fluctuations in cortical potentials and respiration drive fast cortical EEG rhythms in sleeping and waking states. *Clin. Neurophysiol.* **156**, 207–219 (2023).
11. Okun, M., Steinmetz, N. A., Lak, A., Dervinis, M. & Harris, K. D. Distinct Structure of Cortical Population Activity on Fast and Infra-slow Timescales. *Cereb. Cortex* **29**, 2196–2210 (2019).
12. Raut, R. V. *et al.* Arousal as a universal embedding for spatiotemporal brain dynamics. 2023.11.06.565918 Preprint at https://doi.org/10.1101/2023.11.06.565918 (2023).
13. He, B. J., Snyder, A. Z., Zempel, J. M., Smyth, M. D. & Raichle, M. E. Electrophysiological correlates of the brain's intrinsic large-scale functional architecture. *Proc. Natl. Acad. Sci.* **105**, 16039–16044 (2008).

14. Liu, X., Leopold, D. A. & Yang, Y. Single-neuron firing cascades underlie global spontaneous brain events. *Proc. Natl. Acad. Sci.* **118**, e2105395118 (2021).
15. Leopold, D. A., Murayama, Y. & Logothetis, N. K. Very Slow Activity Fluctuations in Monkey Visual Cortex: Implications for Functional Brain Imaging. *Cereb. Cortex* **13**, 422–433 (2003).
16. Collins, L., Francis, J., Emanuel, B. & McCormick, D. A. Cholinergic and noradrenergic axonal activity contains a behavioral-state signal that is coordinated across the dorsal cortex. *eLife* **12**, e81826 (2023).
17. Nazari, M. *et al.* Regional variation in cholinergic terminal activity determines the non-uniform occurrence of cortical slow waves during REM sleep in mice. *Cell Rep.* **42**, 112450 (2023).
18. Zhang, Y. *et al.* Cholinergic suppression of hippocampal sharp-wave ripples impairs working memory. *Proc. Natl. Acad. Sci.* **118**, e2016432118 (2021).
19. Obrig, H. *et al.* Spontaneous Low Frequency Oscillations of Cerebral Hemodynamics and Metabolism in Human Adults. *NeuroImage* **12**, 623–639 (2000).
20. Raut, R. V. *et al.* Global waves synchronize the brain's functional systems with fluctuating arousal. *Sci. Adv.* **7**, eabf2709 (2021).
21. Mitra, A. *et al.* Spontaneous Infra-slow Brain Activity Has Unique Spatiotemporal Dynamics and Laminar Structure. *Neuron* **98**, 297-305.e6 (2018).
22. Chan, A. W., Mohajerani, M. H., LeDue, J. M., Wang, Y. T. & Murphy, T. H. Mesoscale infra-slow spontaneous membrane potential fluctuations recapitulate high-frequency activity cortical motifs. *Nat. Commun.* **6**, 7738 (2015).
23. Ma, Y. *et al.* Resting-state hemodynamics are spatiotemporally coupled to synchronized and symmetric neural activity in excitatory neurons. *Proc. Natl. Acad. Sci. U. S. A.* **113**, E8463–E8471 (2016).
24. Buzsáki, G., Logothetis, N. & Singer, W. Scaling Brain Size, Keeping Timing: Evolutionary Preservation of Brain Rhythms. *Neuron* **80**, 751–764 (2013).

1162 25. Pesaran, B. *et al.* Investigating large-scale brain dynamics using field potential recordings:
1163 analysis and interpretation. *Nat. Neurosci.* **21**, 903–919 (2018).
1164 26. Aladjalova, N. A. Infra-Slow Rhythmic Oscillations of The Steady Potential of the Cerebral Cortex.
1165 *Nature* **179**, 957–959 (1957).
1166 27. Caspers, H. Part I. Relations of steady potential shifts in the cortex to the wakefulness-sleep
1167 spectrum. in *Brain Function. Proceedings of the First Conference, 1961* (ed. Brazier, M. A. B.)
1168 177–214 (University of California Press, 1963).
1169 28. Caspers, H., Speckmann, E.-J. & Lehmenkühler, A. Electrogenesis of Slow Potentials of the Brain.
1170 in *Self-Regulation of the Brain and Behavior* (eds. Elbert, T., Rockstroh, B., Lutzenberger, W. &
1171 Birbaumer, N.) 26–41 (Springer Berlin Heidelberg, Berlin, Heidelberg, 1984).
1172 29. Tabushi, K., Hishikawa, Y., Ueyama, M. & Kaneko, Z. Cortical D.C. potential changes associated
1173 with spontaneous sleep in cat. *Arch. Ital. Biol.* **104**, 152–162 (1966).
1174 30. A, A., M, M. & K, M. [Slow oscillations of potentials observed in the cerebral cortex from the
1175 effect of stimulation of the reticular substaance of the brain stem]. *Boll. Della Soc. Ital. Biol.*
1176 *Sper.* **32**, (1956).
1177 31. Dondey, M. & Snider, R. S. Slow potential shifts following cerebellar stimulation.
1178 *Electroencephalogr. Clin. Neurophysiol.* **7**, 265–272 (1955).
1179 32. Brookhart, J. M., Arduini, A., Mancia, M. & Moruzzi, G. Thalamocortical relations as revealed by
1180 induced slow potential changes. *J. Neurophysiol.* **21**, 499–525 (1958).
1181 33. O'Leary, J. L. & Goldring, S. D-C Potentials of the Brain. *Physiol. Rev.* **44**, 91–125 (1964).
1182 34. Chatrian, G. E., Somasundaram, M. & Tassinari, C. A. DC changes recorded transcranially during
1183 "typical" three per second spike and wave discharges in man. *Epilepsia* **9**, 185–209 (1968).
1184 35. Speckmann, E.-J., Bingmann, D., Lehmenkühler, A. & Lipinski, H. G. Changes of the Bioelectrical
1185 Activity and Extracellular Micromilieu in the Central Nervous System During Variations of Local
1186 Oxygen Pressure. in *Oxygen Sensing in Tissues* (ed. Acker, H.) 179–191 (Springer Berlin
1187 Heidelberg, Berlin, Heidelberg, 1988).

36. Caspers, H., Speckmann, E.-J. & Lehmenkühler, A. DC potentials of the cerebral cortex: Seizure activity and changes in gas pressures. *Rev. Physiol. Biochem. Pharmacol. Vol. 106 Vol. 106* 127–178 (1987).

37. Rodin, E. & Modur, P. Ictal intracranial infra-slow EEG activity. *Clin. Neurophysiol.* **119**, 2188–2200 (2008).

38. Vanhatalo, S. *et al.* Infra-slow oscillations modulate excitability and interictal epileptic activity in the human cortex during sleep. *Proc. Natl. Acad. Sci.* **101**, 5053–5057 (2004).

39. Kanazawa, K. *et al.* Intracranially recorded ictal direct current shifts may precede high frequency oscillations in human epilepsy. *Clin. Neurophysiol.* **126**, 47–59 (2015).

40. Bonaccini Calia, A. *et al.* Full-bandwidth electrophysiology of seizures and epileptiform activity enabled by flexible graphene microtransistor depth neural probes. *Nat. Nanotechnol. 2021 173* **17**, 301–309 (2021).

41. Vanhatalo, S., Voipio, J. & Kaila, K. Full-band EEG (FbEEG): an emerging standard in electroencephalography. *Clin. Neurophysiol. Off. J. Int. Fed. Clin. Neurophysiol.* **116**, 1–8 (2005).

42. Higgins, C. *et al.* Replay bursts in humans coincide with activation of the default mode and parietal alpha networks. *Neuron* **109**, 882-893.e7 (2021).

43. Pedrosa, R. *et al.* Hippocampal ripples coincide with “UP-state” and cortical spindles in Retrosplenial Cortex. 2022.12.19.521088 Preprint at https://doi.org/10.1101/2022.12.19.521088 (2022).

44. Osorio-Forero, A. *et al.* Noradrenergic circuit control of non-REM sleep substates. *Curr. Biol.* **31**, 5009-5023.e7 (2021).

45. Hiltunen, T. *et al.* Infra-slow EEG fluctuations are correlated with resting-state network dynamics in fMRI. *J. Neurosci. Off. J. Soc. Neurosci.* **34**, 356–362 (2014).

46. Londoño-Ramírez, H. *et al.* Multiplexed Surface Electrode Arrays Based on Metal Oxide Thin-Film Electronics for High-Resolution Cortical Mapping. *Adv. Sci.* **11**, 2308507 (2024).

1213 47. Khodagholy, D. *et al.* NeuroGrid: recording action potentials from the surface of the brain. *Nat.*
1214 *Neurosci.* **18**, 310–315 (2015).
1215 48. Khodagholy, D., Gelinas, J. N. & Buzsáki, G. Learning-enhanced coupling between ripple
1216 oscillations in association cortices and hippocampus. *Science* **358**, 369–372 (2017).
1217 49. Tchoe, Y. *et al.* Human brain mapping with multithousand-channel PtNRGrids resolves
1218 spatiotemporal dynamics. *Sci. Transl. Med.* **14**, (2022).
1219 50. Chiang, C.-H. *et al.* Flexible, high-resolution thin-film electrodes for human and animal neural
1220 research. *J. Neural Eng.* **18**, 045009 (2021).
1221 51. Chiang, C.-H. *et al.* Development of a neural interface for high-definition, long-term recording in
1222 rodents and nonhuman primates. *Sci. Transl. Med.* **12**, eaay4682 (2020).
1223 52. Masvidal-Codina, E. *et al.* High-resolution mapping of infra-slow cortical brain activity enabled
1224 by graphene microtransistors. *Nat. Mater.* **18**, 280–288 (2019).
1225 53. Garcia-Cortadella, R. *et al.* Graphene active sensor arrays for long-term and wireless mapping of
1226 wide frequency band epicortical brain activity. *Nat. Commun.* **12**, 1–17 (2021).
1227 54. Cisneros-Fernandez, J. *et al.* A 1024-Channel 10-Bit 36-µW/ch CMOS ROIC for Multiplexed GFET-
1228 Only Sensor Arrays in Brain Mapping. *IEEE Trans. Biomed. Circuits Syst.* **15**, 860–876 (2021).
1229 55. Garcia-Cortadella, R. *et al.* Switchless Multiplexing of Graphene Active Sensor Arrays for Brain
1230 Mapping. *Nano Lett.* acs.nanolett.0c00467 (2020) doi:10.1021/acs.nanolett.0c00467.
1231 56. Schaefer, N. *et al.* Multiplexed neural sensor array of graphene solution-gated field-effect
1232 transistors. *2D Mater.* **7**, 025046 (2020).
1233 57. Moody, W. J., Futamachi, K. J. & Prince, D. A. Extracellular potassium activity during
1234 epileptogenesis. *Exp. Neurol.* **42**, 248–263 (1974).
1235 58. Seigneur, J., Kroeger, D., Nita, D. A. & Amzica, F. Cholinergic Action on Cortical Glial Cells In Vivo.
1236 *Cereb. Cortex* **16**, 655–668 (2006).
1237 59. Böhler, C. *et al.* Multilayer Arrays for Neurotechnology Applications (MANTA): Chronically Stable
1238 Thin-Film Intracortical Implants. *Adv. Sci.* **10**, 2207576 (2023).

1239 60. Chung, J. E. *et al.* High-Density, Long-Lasting, and Multi-region Electrophysiological Recordings
1240 Using Polymer Electrode Arrays. *Neuron* **101**, 21-31.e5 (2019).
1241 61. Over and above frequency: Gamma oscillations as units of neural circuit operations -
1242 ScienceDirect.
1243 https://www.sciencedirect.com/science/article/pii/S0896627323001307?via%3Dihub.
1244 62. Gervasoni, D. *et al.* Global forebrain dynamics predict rat behavioral states and their transitions.
1245 *J. Neurosci. Off. J. Soc. Neurosci.* **24**, 11137–11147 (2004).
1246 63. Sirota, A. *et al.* Entrainment of neocortical neurons and gamma oscillations by the hippocampal
1247 theta rhythm. *Neuron* **60**, 683–697 (2008).
1248 64. Taylor, J. A. *et al.* Spontaneous Recurrent Absence Seizure-like Events in Wild-Caught Rats. *J.*
1249 *Neurosci.* **39**, 4829–4841 (2019).
1250 65. Shaw, F.-Z. Is Spontaneous High-Voltage Rhythmic Spike Discharge in Long Evans Rats an
1251 Absence-Like Seizure Activity? *J. Neurophysiol.* **91**, 63–77 (2004).
1252 66. Duntley, S. P., Kim, A. H., Silbergeld, D. L. & Miller, J. W. Characterization of the mu rhythm
1253 during rapid eye movement sleep. *Clin. Neurophysiol. Off. J. Int. Fed. Clin. Neurophysiol.* **112**,
1254 528–531 (2001).
1255 67. Kozák, G., Földi, T. & Berényi, A. Spike-and-Wave Discharges Are Not Pathological Sleep Spindles,
1256 Network-Level Aspects of Age-Dependent Absence Seizure Development in Rats. *eNeuro* **7**,
1257 0253–19.2019 (2020).
1258 68. Gumnit, R. J. & Takahashi, T. Changes in direct current activity during experimental focal
1259 seizures. *Electroencephalogr. Clin. Neurophysiol.* **19**, 63–74 (1965).
1260 69. Kovac, S., Speckmann, E.-J. & Gorji, A. Uncensored EEG: The role of DC potentials in
1261 neurobiology of the brain. *Prog. Neurobiol.* **165–167**, 51–65 (2018).
1262 70. Reimer, J. *et al.* Pupil fluctuations track rapid changes in adrenergic and cholinergic activity in
1263 cortex. *Nat. Commun.* **7**, 13289 (2016).

71. Lecci, S. *et al.* Coordinated infra-slow neural and cardiac oscillations mark fragility and offline periods in mammalian sleep. *Sci. Adv.* **3**, e1602026 (2017).

72. Yüzgeç, Ö., Prsa, M., Zimmermann, R. & Huber, D. Pupil Size Coupling to Cortical States Protects the Stability of Deep Sleep via Parasympathetic Modulation. *Curr. Biol.* **28**, 392-400.e3 (2018).

73. Cooper, C. *et al.* Ultraslow serotonin oscillations in the hippocampus delineate substates across NREM and waking. 2024.07.09.602643 Preprint at https://doi.org/10.1101/2024.07.09.602643 (2024).

74. Marshall, L., Mölle, M., Michaelsen, S., Fehm, H. L. & Born, J. Slow Potential Shifts at Sleep—Wake Transitions and Shifts Between NREM and REM Sleep. *Sleep* **19**, 145–151 (1996).

75. Nourhashemi, M., Mahmoudzadeh, M., Heberle, C. & Wallois, F. Preictal neuronal and vascular activity precedes the onset of childhood absence seizure: direct current potential shifts and their correlation with hemodynamic activity. *Neurophotonics* **10**, (2023).

76. Contreras, D. & Steriade, M. Spindle oscillation in cats: the role of corticothalamic feedback in a thalamically generated rhythm. *J. Physiol.* **490**, 159–179 (1996).

77. Amzica, F. & Steriade, M. The K-complex: its slow (<1-Hz) rhythmicity and relation to delta waves. *Neurology* **49**, 952–959 (1997).

78. Sirota, A. & Buzsáki, G. Interaction between neocortical and hippocampal networks via slow oscillations. *Thalamus Relat. Syst.* **3**, 245 (2005).

79. Helfrich, R. F., Mander, B. A., Jagust, W. J., Knight, R. T. & Walker, M. P. Old Brains Come Uncoupled in Sleep: Slow Wave-Spindle Synchrony, Brain Atrophy, and Forgetting. *Neuron* **97**, 221-230.e4 (2018).

80. Distinction between slow waves and delta waves sheds light to sleep homeostasis and their association to hippocampal sharp waves ripples | bioRxiv. https://www.biorxiv.org/content/10.1101/2022.12.27.522034v1.abstract.

81. Global waves synchronize the brain's functional systems with fluctuating arousal | Science Advances. https://www.science.org/doi/10.1126/sciadv.abf2709.

82. Lu, H. *et al.* Rat brains also have a default mode network. *Proc. Natl. Acad. Sci.* **109**, 3979–3984 (2012).

83. Watson, B. O., Levenstein, D., Greene, J. P., Gelinas, J. N. & Buzsáki, G. Network Homeostasis and State Dynamics of Neocortical Sleep. *Neuron* **90**, 839–852 (2016).

84. Stitt, I. *et al.* Dynamic reconfiguration of cortical functional connectivity across brain states. *Sci. Rep.* **7**, 8797 (2017).

85. McCormick, D. A., Nestvogel, D. B. & He, B. J. Neuromodulation of Brain State and Behavior. *Annu. Rev. Neurosci.* **43**, 391–415 (2020).

86. Lee, S.-H. & Dan, Y. Neuromodulation of Brain States. *Neuron* **76**, 209–222 (2012).

87. Buzsáki, G., Anastassiou, C. A. & Koch, C. The origin of extracellular fields and currents — EEG, ECoG, LFP and spikes. *Nat. Rev. Neurosci. 2012 136* **13**, 407–420 (2012).

88. Nir, Y. *et al.* Regional Slow Waves and Spindles in Human Sleep. *Neuron* **70**, 153–169 (2011).

89. Vyazovskiy, V. V. *et al.* Local sleep in awake rats. *Nature* **472**, 443–447 (2011).

90. Molinari, S. & Foulkes, D. Tonic and Phasic Events during Sleep: Psychological Correlates and Implications. *Percept. Mot. Skills* **29**, 343–368 (1969).

91. Bueno-Junior, L. S., Ruckstuhl, M. S., Lim, M. M. & Watson, B. O. The temporal structure of REM sleep shows minute-scale fluctuations across brain and body in mice and humans. *Proc. Natl. Acad. Sci.* **120**, e2213438120 (2023).

92. Simor, P., Van Der Wijk, G., Nobili, L. & Peigneux, P. The microstructure of REM sleep: Why phasic and tonic? *Sleep Med. Rev.* **52**, 101305 (2020).

93. Terzano, M. G. *et al.* The Cyclic Alternating Pattern as a Physiologic Component of Normal NREM Sleep. *Sleep* **8**, 137–145 (1985).

94. Halász, P. Hierarchy of MA and the microstructure of sleep. *Neurophysiol. Clin. Neurophysiol.* **28**, 461–475 (1998).

95. Jobert, M., Poiseau, E., Jähnig, P., Schulz, H. & Kubicki, S. Topographical Analysis of Sleep Spindle Activity. *Neuropsychobiology* **26**, 210–217 (1992).

96. Mölle, M., Bergmann, T. O., Marshall, L. & Born, J. Fast and Slow Spindles during the Sleep Slow Oscillation: Disparate Coalescence and Engagement in Memory Processing. *Sleep* **34**, 1411–1421 (2011).

97. Piantoni, G., Halgren, E. & Cash, S. S. Spatiotemporal characteristics of sleep spindles depend on cortical location. *NeuroImage* **146**, 236–245 (2017).

98. Kim, D., Hwang, E., Lee, M., Sung, H. & Choi, J. H. Characterization of Topographically Specific Sleep Spindles in Mice. *Sleep* **38**, 85.

99. Sirota, A. *et al.* Entrainment of Neocortical Neurons and Gamma Oscillations by the Hippocampal Theta Rhythm. *Neuron* **60**, 683–697 (2008).

100. Sherman, M. A. *et al.* Neural mechanisms of transient neocortical beta rhythms: Converging evidence from humans, computational modeling, monkeys, and mice. *Proc. Natl. Acad. Sci.* **113**, (2016).

101. Karvat, G., Alyahyay, M. & Diester, I. Spontaneous activity competes with externally evoked responses in sensory cortex. *Proc. Natl. Acad. Sci.* **118**, e2023286118 (2021).

102. Bagur, S. *et al.* Harnessing olfactory bulb oscillations to perform fully brain-based sleep-scoring and real-time monitoring of anaesthesia depth. *PLOS Biol.* **16**, e2005458 (2018).

103. Karalis, N. & Sirota, A. Breathing coordinates cortico-hippocampal dynamics in mice during offline states. *Nat. Commun.* **13**, 467 (2022).

104. Montgomery, S. M., Betancur, M. I. & Buzsáki, G. Behavior-Dependent Coordination of Multiple Theta Dipoles in the Hippocampus. *J. Neurosci.* **29**, 1381–1394 (2009).

105. Mizuseki, K., Sirota, A., Pastalkova, E. & Buzsáki, G. Theta Oscillations Provide Temporal Windows for Local Circuit Computation in the Entorhinal-Hippocampal Loop. *Neuron* **64**, 267–280 (2009).

106. Lubenov, E. V. & Siapas, A. G. Hippocampal theta oscillations are travelling waves. *Nature* **459**, 534–539 (2009).

1341 107. Patel, J., Fujisawa, S., Berényi, A., Royer, S. & Buzsáki, G. Traveling Theta Waves along the
1342 Entire Septotemporal Axis of the Hippocampus. *Neuron* **75**, 410–417 (2012).
1343 108. Mikulovic, S. *et al.* Ventral hippocampal OLM cells control type 2 theta oscillations and
1344 response to predator odor. *Nat. Commun.* **9**, 3638 (2018).
1345 109. Adhikari, A., Topiwala, M. A. & Gordon, J. A. Synchronized Activity between the Ventral
1346 Hippocampus and the Medial Prefrontal Cortex during Anxiety. *Neuron* **65**, 257–269 (2010).
1347 110. Tort, A. B. L. *et al.* Parallel detection of theta and respiration-coupled oscillations throughout
1348 the mouse brain. *Sci. Rep.* **8**, 6432 (2018).
1349 111. Taylor, J. A., Smith, Z. Z. & Barth, D. S. Spike-wave discharges in Sprague–Dawley rats reflect
1350 precise intra- and interhemispheric synchronization of somatosensory cortex. *J. Neurophysiol.*
1351 **128**, 1152–1167 (2022).
1352 112. Ikeda, A. Focal ictal direct current shifts in humanepilepsy as studied by subdural and scalp
1353 recording. *Brain* **122**, 827–838 (1999).
1354 113. Yang, Y. *et al.* Modelling and prediction of the dynamic responses of large-scale brain
1355 networks during direct electrical stimulation. *Nat. Biomed. Eng.* **5**, 324–345 (2021).
1356 114. John, E. R., Prichep, L. S., Fridman, J. & Easton, P. Neurometrics: Computer-Assisted
1357 Differential Diagnosis of Brain Dysfunctions. *Science* **239**, 162–169 (1988).
1358 115. Basu, I. *et al.* Consistent linear and non-linear responses to invasive electrical brain
1359 stimulation across individuals and primate species with implanted electrodes. *Brain Stimulat.* **12**,
1360 877–892 (2019).
1361 116. Ashkan, K., Rogers, P., Bergman, H. & Ughratdar, I. Insights into the mechanisms of deep
1362 brain stimulation. *Nat. Rev. Neurol.* **13**, 548–554 (2017).
1363 117. Othmer, S., Othmer, S. F., Kaiser, D. A. & Putman, J. Endogenous Neuromodulation at
1364 Infralow Frequencies. *Semin. Pediatr. Neurol.* **20**, 246–257 (2013).

118. Rabiller, G., He, J.-W., Nishijima, Y., Wong, A. & Liu, J. Perturbation of Brain Oscillations after Ischemic Stroke: A Potential Biomarker for Post-Stroke Function and Therapy. *Int. J. Mol. Sci.* **16**, 25605–25640 (2015).

119. Vinokurova, D. E. Ultraslow Signals in Stroke Diagnostics. *J. Evol. Biochem. Physiol.* **61**, 12–30 (2025).

120. Gantenbein, A. R. & Sándor, P. S. Physiological Parameters as Biomarkers of Migraine. *Headache J. Head Face Pain* **46**, 1069–1074 (2006).

121. Cherian, R. & Kanaga, E. G. Theoretical and methodological analysis of EEG based seizure detection and prediction: An exhaustive review. *J. Neurosci. Methods* **369**, 109483 (2022).

122. Zygierewicz, J. High resolution study of sleep spindles. *Clin. Neurophysiol.* **110**, 2136–2147 (1999).

123. Andrillon, T. *et al.* Sleep Spindles in Humans: Insights from Intracranial EEG and Unit Recordings. *J. Neurosci.* **31**, 17821–17834 (2011).

124. Cox, R., Schapiro, A. C., Manoach, D. S. & Stickgold, R. Individual Differences in Frequency and Topography of Slow and Fast Sleep Spindles. *Front. Hum. Neurosci.* **11**, 433 (2017).

125. Dehghani, N., Cash, S. S. & Halgren, E. Topographical frequency dynamics within EEG and MEG sleep spindles. *Clin. Neurophysiol.* **122**, 229–235 (2011).

126. Blanco-Duque, C. *et al.* Oscillatory-Quality of sleep spindles links brain state with sleep regulation and function. *Sci. Adv.* **10**, eadn6247 (2024).

127. Stokes, P. A. *et al.* Transient oscillation dynamics during sleep provide a robust basis for electroencephalographic phenotyping and biomarker identification. *Sleep* **46**, zsac223 (2023).

128. Fernandez-Ruiz, A., Sirota, A., Lopes-dos-Santos, V. & Dupret, D. Over and above frequency: Gamma oscillations as units of neural circuit operations. *Neuron* **111**, 936–953 (2023).

129. Meyerolbersleben, L. S., Sirota, A. & Busse, L. Anatomically resolved oscillatory bursts orchestrate visual thalamocortical activity during naturalistic stimulus viewing. *Neuron* in press (2025).

130. Sirota, A., Csicsvari, J., Buhl, D. & Buzsáki, G. Communication between neocortex and hippocampus during sleep in rodents. *Proc. Natl. Acad. Sci. U. S. A.* **100**, 2065–2069 (2003).

131. Maingret, N., Girardeau, G., Todorova, R., Goutierre, M. & Zugaro, M. Hippocampo-cortical coupling mediates memory consolidation during sleep. *Nat. Neurosci.* **19**, 959–964 (2016).

132. Kim, J., Gulati, T. & Ganguly, K. Competing Roles of Slow-Oscillations and Delta-Waves in Memory Consolidation Versus Forgetting. *Cell* **179**, 514-526.e13 (2019).

133. Peyrache, A., Khamassi, M., Benchenane, K., Wiener, S. I. & Battaglia, F. P. Replay of rule-learning related neural patterns in the prefrontal cortex during sleep. *Nat. Neurosci.* **12**, 919–926 (2009).

134. Clemens, Z. *et al.* Fine-tuned coupling between human parahippocampal ripples and sleep spindles. *Eur. J. Neurosci.* **33**, 511–520 (2011).

135. Massimini, M., Huber, R., Ferrarelli, F., Hill, S. & Tononi, G. The Sleep Slow Oscillation as a Traveling Wave. *J. Neurosci.* **24**, 6862–6870 (2004).

136. Steriade, M. Synchronized activities of coupled oscillators in the cerebral cortex and thalamus at different levels of vigilance [published erratum appears in Cereb Cortex 1997 Dec;7(8):779]. *Cereb. Cortex* **7**, 583–604 (1997).

137. Swanson, R. A. *et al.* Topography of putative bi-directional interaction between hippocampal sharp-wave ripples and neocortical slow oscillations. *Neuron* **113**, 754-768.e9 (2025).

138. Pedrosa, R. *et al.* Hippocampal ripples coincide with “UP-state” and spindles in retrosplenial cortex. *Cereb. Cortex* **34**, bhae083 (2024).

139. Kandel, A. & Buzsáki, G. Cellular–Synaptic Generation of Sleep Spindles, Spike-and-Wave Discharges, and Evoked Thalamocortical Responses in the Neocortex of the Rat. *J. Neurosci.* **17**, 6783–6797 (1997).

140. Amzica, F. & Steriade, M. Cellular substrates and laminar profile of sleep K-complex. *Neuroscience* **82**, 671–686 (1997).

1416 141. Cossart, R., Aronov, D. & Yuste, R. Attractor dynamics of network UP-states in the neocortex.
1417 *Nature* **423**, 283–288 (2003).
1418 142. Ode, K. L., Katsumata, T., Tone, D. & Ueda, H. R. Fast and slow Ca2+-dependent
1419 hyperpolarization mechanisms connect membrane potential and sleep homeostasis. *Curr. Opin.*
1420 *Neurobiol.* **44**, 212–221 (2017).
1421 143. Metherate, R. & Ashe, J. Ionic flux contributions to neocortical slow waves and nucleus
1422 basalis- mediated activation: whole-cell recordings in vivo. *J. Neurosci.* **13**, 5312–5323 (1993).
1423 144. Steriade, M., Amzica, F. & Nunez, A. Cholinergic and noradrenergic modulation of the slow
1424 (approximately 0.3 Hz) oscillation in neocortical cells. *J. Neurophysiol.* **70**, 1385–1400 (1993).
1425 145. Timofeev, I., Grenier, F. & Steriade, M. Disfacilitation and active inhibition in the neocortex
1426 during the natural sleep-wake cycle: An intracellular study. *Proc. Natl. Acad. Sci.* **98**, 1924–1929
1427 (2001).
1428 146. Day, M. *et al.* Dendritic excitability of mouse frontal cortex pyramidal neurons is shaped by
1429 the interaction among HCN, Kir2, and Kleak channels. *J. Neurosci. Off. J. Soc. Neurosci.* **25**, 8776–
1430 8787 (2005).
1431 147. Cunningham, M. O. *et al.* Neuronal metabolism governs cortical network response state.
1432 *Proc. Natl. Acad. Sci.* **103**, 5597–5601 (2006).
1433 148. Tatsuki, F. *et al.* Involvement of Ca2+-Dependent Hyperpolarization in Sleep Duration in
1434 Mammals. *Neuron* **90**, 70–85 (2016).
1435 149. Rasmussen, R., Jensen, M. H. & Heltberg, M. L. Chaotic Dynamics Mediate Brain State
1436 Transitions, Driven by Changes in Extracellular Ion Concentrations. *Cell Syst.* **5**, 591-603.e4
1437 (2017).
1438 150. Tinker, A., Aziz, Q., Li, Y. & Specterman, M. ATP-Sensitive Potassium Channels and Their
1439 Physiological and Pathophysiological Roles. *Compr. Physiol.* **8**, 1463–1511 (2018).
1440 151. Muheim, C. M. *et al.* Dynamic- and Frequency-Specific Regulation of Sleep Oscillations by
1441 Cortical Potassium Channels. *Curr. Biol.* **29**, 2983-2992.e3 (2019).

1442 152. Constantino, N. J. *et al.* ATP-sensitive potassium channels alter glycolytic flux to modulate
1443 cortical activity and sleep. *Proc. Natl. Acad. Sci. U. S. A.* **122**, e2416578122 (2025).
1444 153. Sakata, S. & Harris, K. D. Laminar Structure of Spontaneous and Sensory-Evoked Population
1445 Activity in Auditory Cortex. *Neuron* **64**, 404–418 (2009).
1446 154. Lőrincz, M. L. *et al.* A distinct class of slow (~0.2-2 Hz) intrinsically bursting layer 5 pyramidal
1447 neurons determines UP/DOWN-state dynamics in the neocortex. *J. Neurosci. Off. J. Soc.*
1448 *Neurosci.* **35**, 5442–5458 (2015).
1449 155. Schubert, D., Kötter, R. & Staiger, J. F. Mapping functional connectivity in barrel-related
1450 columns reveals layer- and cell type-specific microcircuits. *Brain Struct. Funct.* **212**, 107–119
1451 (2007).
1452 156. Senzai, Y., Fernandez-Ruiz, A. & Buzsáki, G. Layer-Specific Physiological Features and
1453 Interlaminar Interactions in the Primary Visual Cortex of the Mouse. *Neuron* **101**, 500-513.e5
1454 (2019).
1455 157. Forrest, M. D. The sodium-potassium pump is an information processing element in brain
1456 computation. *Front. Physiol.* **5**, 472 (2014).
1457 158. Lux, H. D. & Neher, E. The equilibration time course of [K+]0 in cat cortex. *Exp. Brain Res.* **17**,
1458 (1973).
1459 159. Prince, D. A., Lux, H. D. & Neher, E. Measurement of extracellular potassium activity in cat
1460 cortex. *Brain Res.* **50**, 489–495 (1973).
1461 160. Futamachi, K. J., Mutani, R. & Prince, D. A. Potassium activity in rabbit cortex. *Brain Res.* **75**,
1462 5–25 (1974).
1463 161. Krishnan, G. P., Filatov, G., Shilnikov, A. & Bazhenov, M. Electrogenic properties of the Na^+
1464 /K^+ ATPase control transitions between normal and pathological brain states. *J. Neurophysiol.*
1465 **113**, 3356–3374 (2015).

162. Krishnan, G. P., Filatov, G., Shilnikov, A. & Bazhenov, M. Electrogenic properties of the Na^+/K^+ ATPase control transitions between normal and pathological brain states. *J. Neurophysiol.* **113**, 3356–3374 (2015).

163. Gumnit, R. J., Matsumoto, H. & Vasconetto, C. DC activity in the depth of an experimental epiletic focus. *Electroencephalogr. Clin. Neurophysiol.* **28**, 333–339 (1970).

164. Nikulin, V. V. *et al.* Monochromatic Ultra-Slow (~0.1Hz) Oscillations in the human electroencephalogram and their relation to hemodynamics. *NeuroImage* **97**, 71–80 (2014).

165. Raichle, M. E. Two views of brain function. *Trends Cogn. Sci.* **14**, 180–190 (2010).

166. Grooms, J. K. *et al.* Infra-slow Electroencephalographic and Dynamic Resting State Network Activity. *Brain Connect.* **7**, 265–280 (2017).

167. He, B. J. & Raichle, M. E. The fMRI signal, slow cortical potential and consciousness. *Trends Cogn. Sci.* **13**, 302–309 (2009).

168. Wang, Z. *et al.* REM sleep is associated with distinct global cortical dynamics and controlled by occipital cortex. *Nat. Commun.* **13**, 6896 (2022).

169. Yu, Y. *et al.* Sleep fMRI with simultaneous electrophysiology at 9.4 T in male mice. *Nat. Commun.* **14**, 1651 (2023).

170. Nazari, M. *et al.* Regional variation in cholinergic terminal activity determines the non-uniform occurrence of cortical slow waves during REM sleep in mice. *Cell Rep.* **42**, 112450 (2023).

171. Osorio-Forero, A. *et al.* Infra-slow noradrenergic locus coeruleus activity fluctuations are gatekeepers of the NREM–REM sleep cycle. *Nat. Neurosci.* **28**, 84–96 (2025).

172. Siapas, A. G. & Wilson, M. A. Coordinated Interactions between Hippocampal Ripples and Cortical Spindles during Slow-Wave Sleep. *Neuron* **21**, 1123–1128 (1998).

173. Sirota, A., Csicsvari, J., Buhl, D. & Buzsáki, G. Communication between neocortex and hippocampus during sleep in rodents. *Proc. Natl. Acad. Sci.* **100**, 2065–2069 (2003).

174. Battaglia, F. P., Sutherland, G. R. & McNaughton, B. L. Hippocampal sharp wave bursts coincide with neocortical “UP-state” transitions. *Learn. Mem.* **11**, 697–704 (2004).

175. Logothetis, N. K. *et al.* Hippocampal–cortical interaction during periods of subcortical silence. *Nature* **491**, 547–553 (2012).

176. Kaplan, R. *et al.* Hippocampal Sharp-Wave Ripples Influence Selective Activation of the Default Mode Network. *Curr. Biol.* **26**, 686–691 (2016).

177. Herreras, O. Local field potentials: Myths and misunderstandings. *Front. Neural Circuits* **10**, 101 (2016).

178. Buzsaki, G. *et al.* Nucleus basalis and thalamic control of neocortical activity in the freely moving rat. *J. Neurosci.* **8**, 4007–4026 (1988).

179. Rasmussen, R. *et al.* Cortex-wide Changes in Extracellular Potassium Ions Parallel Brain State Transitions in Awake Behaving Mice. *Cell Rep.* **28**, 1182-1194.e4 (2019).

180. Dietz, A. G. *et al.* Local extracellular K+ in cortex regulates norepinephrine levels, network state, and behavioral output. *Proc. Natl. Acad. Sci.* **120**, e2305071120 (2023).

181. Brankačk, J., Stewart, M. & E. Fox, S. Current source density analysis of the hippocampal theta rhythm: associated sustained potentials and candidate synaptic generators. *Brain Res.* **615**, 310–327 (1993).

182. Fox, M. D. *et al.* The human brain is intrinsically organized into dynamic, anticorrelated functional networks. *Proc. Natl. Acad. Sci.* **102**, 9673–9678 (2005).

183. Rayshubskiy, A. *et al.* Direct, intraoperative observation of ~ 0.1 Hz hemodynamic oscillations in awake human cortex: Implications for fMRI. *NeuroImage* **87**, 323–331 (2014).

184. Power, J. D., Schlaggar, B. L. & Petersen, S. E. Studying Brain Organization via Spontaneous fMRI Signal. *Neuron* **84**, 681–696 (2014).

185. Golanov, E. V., Yamamoto, S. & Reis, D. J. Spontaneous waves of cerebral blood flow associated with a pattern of electrocortical activity. *Am. J. Physiol.-Regul. Integr. Comp. Physiol.* **266**, R204–R214 (1994).

1517 186. Julien, C. The enigma of Mayer waves: Facts and models. *Cardiovasc. Res.* **70**, 12–21 (2006).
1518 187. Nikulin, V. V. *et al.* Monochromatic Ultra-Slow (~0.1Hz) Oscillations in the human
1519 electroencephalogram and their relation to hemodynamics. *NeuroImage* **97**, 71–80 (2014).
1520 188. Hiltunen, T. *et al.* Infra-Slow EEG Fluctuations Are Correlated with Resting-State Network
1521 Dynamics in fMRI. *J. Neurosci.* **34**, 356–362 (2014).
1522 189. Moore, C. I. & Cao, R. The Hemo-Neural Hypothesis: On The Role of Blood Flow in
1523 Information Processing. *J. Neurophysiol.* **99**, 2035–2047 (2008).
1524 190. Drew, P. J. Neurovascular coupling: motive unknown. *Trends Neurosci.* **45**, 809–819 (2022).
1525 191. Hamel, E. Perivascular nerves and the regulation of cerebrovascular tone. *J. Appl. Physiol.*
1526 **100**, 1059–1064 (2006).
1527 192. Tsai, C.-J. *et al.* Cerebral capillary blood flow upsurge during REM sleep is mediated by A2a
1528 receptors. *Cell Rep.* **36**, 109558 (2021).
1529 193. Bangash, M. F. *et al.* Cerebrovascular Response to Arousal from NREM and REM Sleep. *Sleep*
1530 **31**, 321 (2008).
1531 194. Hauglund, N. L. *et al.* Norepinephrine-mediated slow vasomotion drives glymphatic
1532 clearance during sleep. *Cell* **0**, (2025).
1533 195. Rubehn, B. & Stieglitz, T. In vitro evaluation of the long-term stability of polyimide as a
1534 material for neural implants. *Biomaterials* **31**, 3449–3458 (2010).
1535 196. Hassler, C., Boretius, T. & Stieglitz, T. Polymers for neural implants. *J. Polym. Sci. Part B*
1536 *Polym. Phys.* **49**, 18–33 (2011).
1537 197. Schaefer, N. *et al.* Improved metal-graphene contacts for low-noise, high-density
1538 microtransistor arrays for neural sensing. *Carbon* **161**, 647–655 (2020).
1539 198. Lu, H. *et al.* SU8-based micro neural probe for enhanced chronic in-vivo recording of spike
1540 signals from regenerated axons. in *Proceedings of IEEE Sensors* 66–69 (2006).
1541 doi:10.1109/ICSENS.2007.355719.

199. Márton, G. *et al.* A multimodal, SU-8 - Platinum - Polyimide microelectrode array for chronic in vivo neurophysiology. *PLoS ONE* **10**, (2015).

200. Felix, S. H. *et al.* Insertion of Flexible Neural Probes Using Rigid Stiffeners Attached with Biodissolvable Adhesive. *J. Vis. Exp. JoVE* 50609 (2013) doi:10.3791/50609.

201. Garcia-Cortadella, R. *et al.* Distortion-Free Sensing of Neural Activity Using Graphene Transistors. *Small* **16**, 1906640 (2020).

202. Mitra, P. P. & Pesaran, B. Analysis of Dynamic Brain Imaging Data. *Biophys. J.* **76**, 691–708 (1999).

203. Schmitzer-Torbert, N. & Redish, A. D. Neuronal Activity in the Rodent Dorsal Striatum in Sequential Navigation: Separation of Spatial and Reward Responses on the Multiple T Task. *J. Neurophysiol.* **91**, 2259–2272 (2004).

204. Hyvarinen, A. Fast and robust fixed-point algorithms for independent component analysis. *IEEE Trans. Neural Netw.* **10**, 626–634 (1999).

205. Craig E. Tenke, J. K. Optimizing PCA Methodology for ERP Component Identification and Measurement: Theoretical Rationale and Empirical Evaluation. *Clin. Neurophysiol.* (2003).

206. Benjamini, Y. & Hochberg, Y. Controlling the False Discovery Rate: A Practical and Powerful Approach to Multiple Testing. *J. R. Stat. Soc. Ser. B Methodol.* **57**, 289–300 (1995).

Acknowledgments

We thank Roustem Khazipov and members of Sirota lab for useful discussions. This work has been funded by the European Union's Horizon 2020 research and innovation program under Grant Agreement No. 732032 (BrainCom), Grant Agreement No. 881603 (GrapheneCore3). Research at the LMU was supported by the Bundesministerium für Bildung und Forschung [grant number 01GQ0440]. ICN2 is supported by the Severo Ochoa Centres of Excellence programme, funded by the Spanish Research Agency (AEI, grant no. SEV-2017–0706), and by the CERCA Programme/Generalitat de Catalunya. RGC received funding from the Alexander von Humboldt foundation and the Marie Curie individual fellowship program. This work has made use of the Spanish ICTS Network MICRONANOFABS, partially supported by MICINN and the ICTS 'NANBIOSIS', more specifically by the Micro-NanoTechnology Unit of the CIBER in Bioengineering, Biomaterials and Nanomedicine (CIBER-BBN) at the IMB-CNM. We also acknowledge funding from the Generalitat de Catalunya (2017 SGR 1426), and the 2DTecBio project (FIS2017-85787-R) funded by the Ministerio de Ciencia, Innovación y Universidades of Spain, the Agencia Estatal de Investigación (AEI) and the Fondo Europeo de

Desarrollo Regional (FEDER/UE). Part of this work was co-funded by the European Regional Development Funds (ERDF) allocated to the Programa operatiu FEDER de Catalunya 2014–2020, with the support of the Secretaria d'Universitats i Recerca of the Departament d'Empresa i Coneixement of the Generalitat de Catalunya for emerging technology clusters devoted to the valorization and transfer of research results (GraphCAT 001-P-001702).

Author contributions

RGC contributed to the conceptual development of graphene recording systems, fabrication and characterization of graphene probes, development and execution of surgical procedures, acquisition of electrophysiological recordings, data analysis and manuscript preparation. JCF designed and characterised the ASIC and developed the headstage hardware, data communication protocols and data acquisition software. GS developed the techniques for the chronic implantation of large-scale probes. AS contributed to the factor analysis of sleep spindles. AU contributed to the data pre-processing and analysis of infra-slow dynamics. NS contributed to the conceptual design of graphene recording systems and fabrication of graphene probes. JA contributed to the development of the discrete electronics system for the operation of graphene probes. EMC contributed to the conceptual development of the technology. EDC contributed to the development of the graphene flexible electronics. RM development of electronics for ASIC headstage. JP and MK implemented the firmware for digital data communication. HL developed the software for recording and analysis. CJ and JM tested and validated the operation of the ASIC headstage. XI contributed to the design and fabrication of graphene probes. FSG led the team for the design of the ASIC and headstage. AGB and JAG coordinated the development of graphene recording systems. AS contributed to the conceptual development of the technologies and experiments. Supervised the electrophysiological recordings, data analysis and manuscript preparation.